J. Fluid Mech. (2006), *vol.* 546, *pp.* 255–284.
doi:10.1017/S002211200500710X Printed in the United Kingdom

Wall imprint of turbulent structures and heat transfer in multiple impinging jet arrays

By LEON F. G. GEERS[1], K. HANJALIĆ[2] AND M. J. TUMMERS[2]

[1]TNO Defense, Safety, and Security, PO Box 45, 2280 AA Rijswijk, The Netherlands
[2]Department of Applied Sciences, Delft University of Technology, PO Box 5046, 2600 GA Delft, The Netherlands

(Received 2 May 2004 and in revised form 5 July 2005)

Thermal imprint and heat transfer on the target surface in multiple impinging jet arrays have been investigated in conjunction with flow pattern and large-scale eddy structure. Surface temperature was measured with liquid crystal thermography (LCT) in a range of jet configurations with hexagonal and in-line orifice arrangements for different combinations of distances between the orifices $s/D_m = 2$–6 and between the orifice plate and the impingement surface $H/D_m = 3$–10 (where D_m is the orifice diameter). The hexagonal arrangement was considered with two different orifice shapes: sharp-edged and contoured. For selected configurations, the distribution of Nusselt number and its peculiarities were analysed in relation with the underlying eddy structure educed by proper orthogonal decomposition (POD) of the snapshots of fluid velocity measured with particle image velocimetry (PIV). Owing to the breakdown of the jets, heat transfer deteriorates with increasing orifice-to-plate distance. The jet interaction and breakdown become more severe as the jets are placed closer to each other. The large-scale eddies originating from the jet-edge shear layers grow as they are convected towards the impingement plate. Eddies of sizes between 0.2 and 0.3 orifice diameters are shown to break up the jets and cause mixing of fresh and spent fluid, lowering the beneficial temperature gradient. In some configurations, an asymmetric flow pattern is generated with embedded weak eddies on only one side of the diagonal symmetry line, which is reflected in an asymmetrical heat transfer distribution on the impingement plate. For $H/D_m > 4$, the Nusselt number shows peak values in and around the jet impingement centres, but relatively uniform distribution of turbulence kinetic energy with local negative energy production close to the impingement surface.

1. Introduction

The design of industrial heat transfer equipment that uses impinging fluid jets to achieve cooling, heating or drying of the product surface, is still based on empirical correlations derived from numerous experiments. These correlations connect the fluid flow rate, the diameter of the nozzles, their spacing and their distance to the target surface, which can be chosen to solve a given heat or mass transfer problem. A review of frequently used correlations can be found, for example, in Viskanta (1993) for both single and multiple impinging jets. Another useful set of generic empirical correlations for a number of basic nozzle geometries has been collected and generalized by Martin (1977) on the basis of correlations published earlier by other workers.

The empirical correlations are usually formulated in terms of Nusselt number as a function of Reynolds number and basic geometrical parameters, such as the

non-dimensional distance between the jets ('pitch') s/D_m and the non-dimensional distance between the nozzle plate and the target surface H/D_m, where D_m is the nozzle diameter. As such, these correlations give no insight into the subtle intricacies of flow and turbulence structure and their effects on heat transfer, which may differ significantly from one set of configuration, nozzle shape, and inflow conditions to another, even for the same Re number, s/D_m, and H/D_m. Moreover, other factors arising from specific conditions of the experimental set-up such as turbulence intensity and distribution in the jets, ambient and outlet boundary conditions, add to the uncertainty in formulating general correlations between geometrical and flow conditions on the one hand and heat transfer rates on the other. Hence, empirical correlations can serve only as a rough guideline for selecting appropriate jet parameters and configuration for specific purposes, and only within the variable range for which the correlation was derived.

To achieve the optimum design of heat transfer equipment, detailed knowledge is required not only of the effect of various bulk flow and configuration parameters, but also of the mechanisms of heat transfer and its effects on the temperature distribution over the target surface. The local heat transfer should reflect the near-wall vortical and turbulence structure, which may vary in different jets configurations, inflow and external conditions. Numerous experiments with single impinging jets have detected ring vortices generated in the shear layer at the jet edges. Aperiodic generation and ejection of coherent vortices and their breakup upon impingement are known to cause strong local fluctuations of the surface temperature that reflect both the removal of warm surface fluid by the vortex ejection process, and the corresponding influx of cool fluid from upstream. However, even in single jets, little is known about their wall imprint, which should play a major role in the wall temperature distribution.

Realizing that the essence of heat transfer enhancement lies in the understanding of flow and turbulence fields, some recent works focused on measuring mean and fluctuating velocities aimed at providing more information about flow and turbulence structure. Kataoka (1990) argued that the surface renewal effect of large-scale eddies impinging on heat transfer surfaces is dominant in the mechanism of heat transfer enhancement in the stagnation point of a single impinging jet. Ring vortices around the jet will grow in the downstream direction of the jet, coalesce and finally break up into large-scale eddies at the end of the jet's potential core region. Additionally, the potential core fluid is alternately accelerated and decelerated owing to the growing ring vortices surrounding the jet, which induces potential core fluctuations. Angioletti *et al.* (2003) provided experimental evidence of the existence of these axial velocity pulsations by means of particle image velocimetry (PIV). They showed, albeit at relatively low Reynolds numbers (1×10^3 to 4×10^3), that the pulsations weaken the boundary-layer stability at stagnation and affect the local heat transfer.

Because of inherent correlation between the surface temperature and the flow structure, control of heat transfer implies control over the formation and breakdown mechanism of large-scale eddies. For impinging jets, different strategies have been studied to accomplish this. Among these is the adaptation of the shape of the orifice or nozzle from which the jet issues. Arjocu & Liburdy (1999) studied the dynamics of a three-by-three elliptic jet array. Using flow visualizations and PIV, the effects of jet aspect ratio, inter-jet spacing, and orifice-to-impingement-plate on the integrated surface-layer vorticity and turbulent length scales were investigated at low Reynolds numbers (300 to 1500). Although the use of vorticity magnitude for the identification of vortical structures is successful in free shear flows, Jeong & Hussain (1995) show that it is not only sensitive to local swirling motion typical for a vortex, but also

to shear. In impinging flows, vorticity will therefore be clouded by the presence of strong shear near the impingement wall, rendering identification methods based on the vorticity magnitude less useful in these flows.

Acoustic or mechanical excitation of the flow is another method to control coherent structure dynamics. By pulsating the flow upstream of a nozzle or orifice, the altered flow structure in the shear layer will significantly change the wall heat transfer. However, the selection of the excitation frequency is important since different excitation frequencies can lead to different flow structures. According to Liu & Sullivan (1996) the initiated intermittent vortex pairing produces a chaotic 'lump eddy' which contains a great deal of the small-scale random turbulence, when the excitation frequency is close to the natural frequency of the impinging jet. These random structures enhance the local heat transfer. When forcing is near a sub-harmonic of the natural frequency, stable vortex pairing is promoted. The strong large-scale well-organized vortices formed after the stable pairing induce the unsteady separation of the wall boundary layer and hence, lead to the local heat transfer reduction. By contrast, Gau, Sheu & Shen (1997) have found that excitation at the natural frequency of the jet or its sub-harmonics will increase the turbulence intensity in both the shear layer and the core and enhances the heat transfer. At non-inherent frequencies, however, the most unstable wave can be suppressed, which reduces the turbulence intensity and decreases the heat transfer. Mladin & Zumbrunnen (1997) conjecture that enhancements can only be obtained under combinations of pulse amplitude and frequency which lie in or near an unstable regime. In other words, having the right excitation frequency is a necessary, but insufficient condition for heat transfer enhancement. The excitation amplitude also has to meet certain requirements.

In contrast to single jets, very little is known about the flow and turbulence structure in multiple jet configurations. Here, the additional factor is the interaction between neighbouring jets, which – depending on their mutual distance – can have a dominant effect on heat transfer intensity, and especially on its distribution over the impingement surface. Most literature dealing with multiple jets reports flow field data in jet arrays of custom-made nozzle arrangements, but few results are available on the measurements of mean flow and turbulence characteristics. For instance, Barata (1996) conducted laser-Doppler anemometry (LDA) measurements and numerical simulations in an arrangement of three jets and studied the effect of crossflow on the jets below a V/STOL (vertical/short take-off and landing) aircraft in ground proximity. Findlay, Salcudean & Gartshore (1999) also investigated jets in a crossflow, but their configuration consisted of a row of square nozzles. Matsumoto *et al.* (1999) examined the flow pattern and the heat transfer from an array of circular impinging jets. Their geometry, consisting of a square array of 5×5 round nozzles, is well suited to serve as a generic configuration, but unfortunately they studied only the qualitative flow features.

Knowing the interaction between turbulent structures in an impinging jet and impingement heat transfer, is the key to mastering control over the heat transfer and thus to improvement of heat transfer efficiency and homogeneity. Therefore, the primary objective of the present investigation is to gain a better understanding of the interaction of the flow and the turbulence structure with the heat transfer in impinging jet arrays. For this purpose, we performed measurements of velocity field in multiple impinging jets using PIV and heat transfer measurements on the impingement surface using liquid crystal thermography (LCT). An attempt has been made to explain the heat transfer non-uniformity and local peculiarities in terms of thermal imprint of vortical structure on the impinging surface. The initial aim was to correlate the

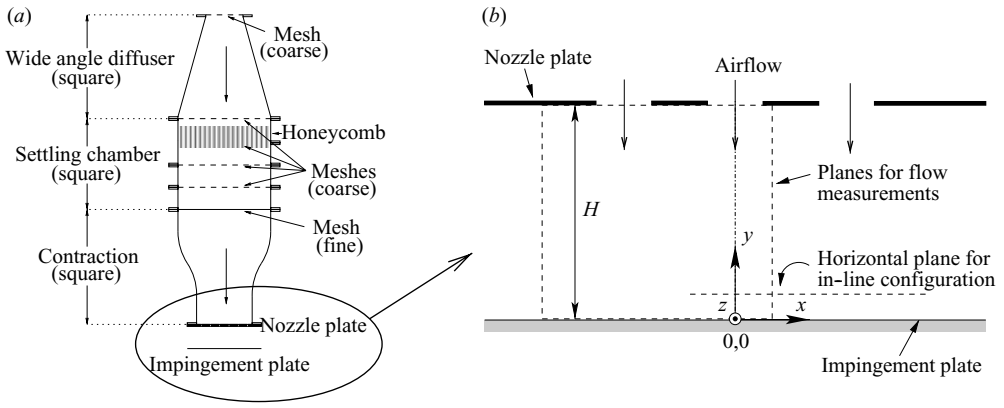

FIGURE 1. (*a*) End section of the wind tunnel and (*b*) flow configuration for all jet arrays.

instantaneous fluid velocity field with the surface temperature field through a series of simultaneous snapshots. However, despite careful coating of the target surface with a very thin layer of liquid crystals of about 15 μm, the LCT response appeared to be too slow to capture turbulent fluctuations of the temperature. Hence the analysis of mutual correlation will be confined to ensemble-averaged fields. We focused in particular on the effects of geometrical parameters on heat transfer distribution and its relation to the underlying flow pattern and vortical structure. The main geometrical parameters considered were the orifice-to-plate spacing, the pitch and the shape of the orifices.

2. Experiments

2.1. *Flow configuration*

In order to ensure reproducible uniform and disturbance-free inflow conditions for all jets, great care was taken to design a special wind tunnel and its test section following the recommendations of Mehta & Bradshaw (1979). Figure 1(*a*) shows the end section of the wind tunnel and a blow-up of a segment of the measurement is shown in figure 1(*b*). Air from the wind tunnel was issued through an orifice plate, after which it impinged on a flat target surface parallel to the orifice plate. The temperature of the jet air was equal to the temperature of the air surrounding the experimental rig. The air temperature in the wind tunnel was monitored using a Pt-100 probe (S1320 series, Systemteknik AB) and the pressure was measured by a micromanometer (FC012, Furness Controls). All physical properties of the air were evaluated at the time-averaged temperature of the jets.

Figure 1(*b*) shows the flow configuration for the jet array flow measurements. Flow measurements were conducted using PIV in planes perpendicular to the orifice and impingement plates and in a plane parallel to the impingement plate. Heat transfer measurements on the impingement plate were conducted using LCT.

The LCT measurements of the temperature on the target surface were performed with two different orifice arrangements: in-line and hexagonal, each for a range of orifice spacings $s/D_m = 2$–6 and orifice to target plate distances $H/D_m = 3$–10. The hexagonal arrangement consists of 13 orifices (figure 2*a*) and the in-line arrangement consists of 3×3 (figure 2*b*). Figure 3 shows two shapes of orifices in the hexagonal arrangement. The sharp orifice plates in figure 3(*a*) consist of aluminium plates with

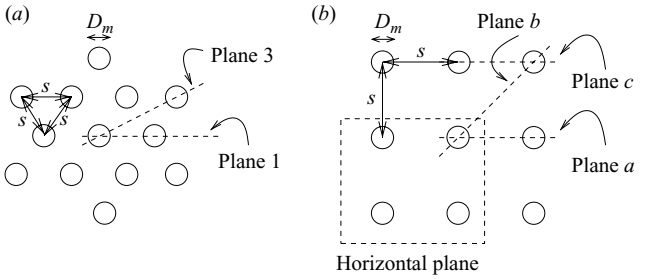

FIGURE 2. Two different arrangements of the orifices in the orifice plates. (*a*) Hexagonal configuration; (*b*) in-line configuration.

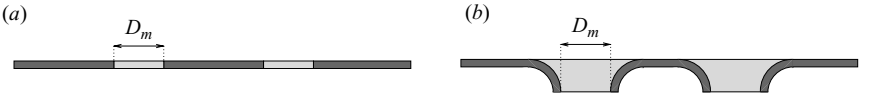

FIGURE 3. Cross-sections of the two orifice shapes. (*a*) Sharp orifices; (*b*) contoured orifices.

bored holes, and the contoured orifice plates in figure 3(*b*) consist of stainless steel plates with holes that are punched, creating a contoured shape. For the in-line orifice arrangement, the orifices were all sharp-edged. The diameter of the orifices D_m was 13 mm for all orifice plates.

The PIV measurements were conducted only for two configurations: the hexagonal orifice arrangement with sharp-edged orifices and an orifice pitch s of $2D_m$, and the in-line orifice arrangement with sharp-edged orifices and $s = 4D_m$. For both configurations, the distance H between the orifice plate and the impingement plate was $4D_m$.

2.2. *Heat transfer measurement system*

Figure 4 shows the experimental rig used for the heat transfer measurements. The air issued from an orifice plate impinges upon a stainless steel (type 304) sheet with a thickness of 25 μm. This sheet is stretched between two clamps. Two cylindrical supports bend the sheet downwards at both ends to prevent the clamps from disturbing the flow. The underside of the sheet is covered by a layer of black backing paint of about 5 μm in thickness and a layer of liquid crystals (BM/R30C20W/C17-10, Hallcrest) of about 15 μm to monitor the temperature of the sheet. The thickness of the liquid crystal layer proved to be sufficient for producing colours with sufficient saturation.

The impingement sheet is heated electrically by means of a current source (Delta Elektronika) that can supply up to 100 A at 4 V. A voltmeter (3465B, Hewlett Packard) measures the voltage drop over the impingement plate, while a combination of a 1 mΩ series resistance and another voltmeter (8000A, Fluke) measure the current through the plate. Four 150 W light sources (DCR III, Schott-Fostec LLC) were used to illuminate the liquid crystals. The light from these sources is guided through four glass fibre bundles and transferred to two 13 in Light Lines (Schott-Fostec, LLC). In these devices the fibres from the bundles are ordered to produce light lines of homogeneous intensity. The infrared radiation that the crystals receive from the light source is reduced to a minimum by an IR-filter before the light is coupled into the fibres. The colour temperature associated with the spectrum of the light is about 3200 K. A PCO

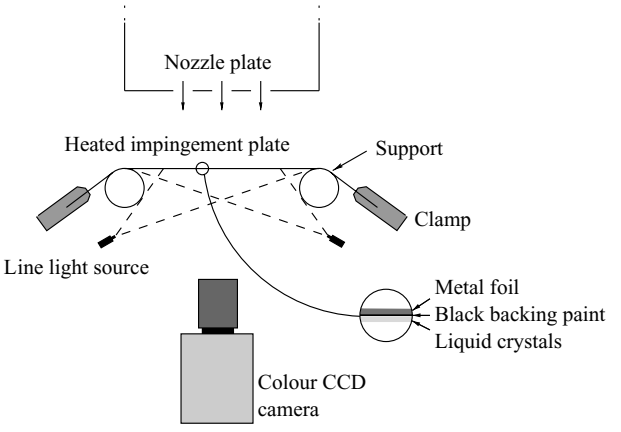

FIGURE 4. Experimental rig for temperature measurements.

Configuration	Nozzle shape	s/D_m	H/D_m	$Re \times 10^3$
Hexagonal	Sharp	2, 4, 6	3, 4, 6, 8, 10	5, 10, 15, 20
	Contoured	2, 4, 6	3, 4, 6, 8, 10	5, 10, 15, 20
In-line	Sharp	4	3, 4, 6, 8, 10	5, 10, 15, 20

TABLE 1. Experimental parameters for all orifice configurations.

SensiCam SVGA colour camera was used to acquire snapshots of the liquid crystals. The camera contains a 2/3 in CCD chip with 1280×1024 pixels that record the intensity of the incident light. The CCD chip is equipped with Bayer filters to distinguish colours.

2.3. *Heat transfer measurements and data analysis*

The three parameters that were varied in the heat transfer experiments are the pitch (s/D_m), the distance between the orifice plate and the impingement plate H/D_m, and the Reynolds number Re. Table 1 presents all possible combinations of the parameters (in total 140) that were studied with LCT.

The acquired images of the liquid crystals were filtered using a median filter (Gonzalez & Woods 2002) to remove random noise that appeared as a result of the non-uniform distribution of the Bayer colour filters on the pixels of the CCD-chip. A top-hat smoothing filter subsequently produced smooth colour images of the liquid crystal surface. After filtering the images, temperatures are determined from the hue values of the colours (Hay & Hollingsworth 1996) by using a lookup table.

The lookup table was created after careful *in situ* calibration of the crystals prior to the heat transfer experiments. By means of a constant-temperature water bath, the impingement foil was kept at a known uniform temperature, while the camera acquired 10 images. After filtering these images and averaging them, hue values were determined for all pixels in the images and these values were stored in the lookup table, together with the temperature at which the images were taken. This was done for about 100 values of the temperature between 32 and 44 °C. A sample of a calibration curve is shown in figure 5(a) with horizontal error bars representing the uncertainty of the hue. This was derived from the standard deviation of the hue resulting from the calibration procedure. Figure 5(b) shows a plot of the uncertainty of the temperature

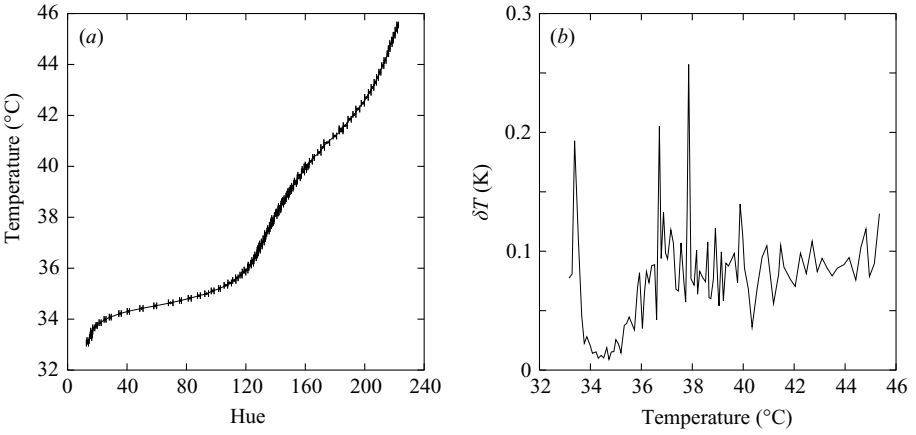

FIGURE 5. Calibration line with measurement error and the error in temperature. (*a*) Calibration with error in hue; (*b*) resulting error in temperature.

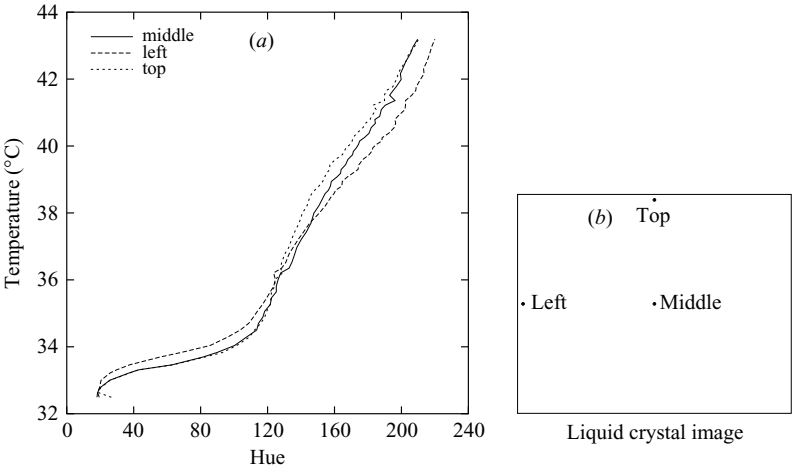

FIGURE 6. Three hue-to-temperature calibration lines at different positions in the image plane. (*a*) Three calibration profiles; (*b*) positions of the profiles.

δT for the whole temperature range, calculated using $\delta T = |\mathrm{d}T/\mathrm{d}H|\delta H$, where $|\mathrm{d}T/\mathrm{d}H|$ is the slope of the calibration curve and δH is the uncertainty of the hue value. The uncertainty is around 0.1 K, i.e. 1 % with respect to the temperature range, which is a typical value for liquid crystals according to Kasagi, Moffat & Hirata (2001). The uncertainties are very low between 34 and 36 °C, because of the high sensitivity in that region: the slope of the calibration curve is very flat.

In figure 6(*a*), three calibration curves are plotted that map hue values to temperatures. These curves were taken at three different positions in the view field of the camera depicted in figure 6(*b*). Although the curves show a similar trend, hue values are mapped onto different temperatures by the three curves. Differences are of the order of 0.9 K at maximum. Given a total range of about 10 K this is a 9 % difference. If only one calibration curve were used for a whole image, errors of this magnitude would be introduced. This is the reason for using a calibration-per-pixel, as was illustrated above.

The values of the impinging jet Nusselt number Nu can be calculated from an energy balance over a small element of the impingement plate. On the top side of the sheet, heat is transferred to the environment by forced convection due to the impinging jets (q_j) and radiation ($q_{r,steel}$). Within the metal sheet, lateral conduction takes place (q_c) and on the underside of the sheet, heat is transferred to the environment by radiation ($q_{r,LC}$) and by convection (q_d). The convection on the bottom of the sheet is caused by possible disturbing (very low velocity) air flows in the laboratory. The sum of all the heat transfer terms is balanced by the heat production through electrical dissipation (q_e) in the metal sheet:

$$q_e = q_j + q_d + q_{r,steel} + q_{r,LC} + q_c. \tag{2.1}$$

The term q_d was considered constant over the impingement sheet. It was estimated using $Nu_d = 0.332 Re_d^{0.5} Pr^{0.33}$ (Janssen & Warmoeskerken 1991) on the basis of a flow velocity of $10\,\mathrm{cm\,s^{-1}}$ and the sheet width as a characteristic length scale for Nu_d and Re_d. Because the conduction term amounts to only 1 % of the total heat transferred in the element, it was not taken into account in the calculation of the impinging jet heat transfer rate. Additionally, because the second derivative of the temperature distribution must be approximated using a finite-difference scheme, the relative uncertainty in the differential estimate will be higher than the relative uncertainty in the temperature distribution. The local impinging jet Nusselt number at position (x, y) on the sheet can be calculated using $Nu(x, y) = q_j/(T(x, y) - T_j)\ D_m/\lambda_{air}$, where $T(x, y)$ is the measured sheet temperature at (x, y), T_j is the jet temperature, and λ_{air} is the heat conduction coefficient of air at T_j.

The heat flux from the liquid crystal layer will cause the temperature of the liquid crystals to be lower than the temperature of the metal sheet. This heat flux equals the sum of the q_d and $q_{r,LC}$ terms that amount to 34 and 179 W $\mathrm{m^{-2}}$, respectively, in the worst case of a 30 K temperature difference between the crystals and the surroundings. On the basis of this heat flux, the temperature difference between the metal sheet and the outer surface of the liquid crystals is estimated to be about 0.016 K in the steady state, i.e. assuming a linear temperature gradient over the paint and crystal layers. This is a negligible difference and it will therefore be ignored.

To assess the dynamic behaviour of the sheet, characteristic time scales of all processes involved in the colour change of the liquid crystals were compared. Rearranging the molecular structure of liquid crystals typically occurs on a time scale of the order of tens of milliseconds (Moffat 1990). The characteristic time scales of the conductive processes in the metal sheet, the backing paint layer and the liquid crystals amount to 160 μs, 10 μs, and 660 μs, respectively. It can therefore be concluded that the liquid crystal temperature is not lagging behind the metal sheet temperature.

Unfortunately, there is a time-scale disparity between the liquid crystal colour change and the dominant heat transfer processes owing to jet impingement: the convective ('surface renewal') time scales of the air flow in the jets lie between 1.9 ms and 7.5 ms for jet Reynolds numbers between 5×10^3 and 20×10^3. The jet Reynolds number is defined here as $Re = U_{CL} D_m/\nu_{air}$, where U_{CL} is the velocity on the centreline of a jet and ν_{air} is the kinematic viscosity of the jet air. The convective time scales were calculated on the basis of a Strouhal number of 0.3, which is a much reported value for the natural oscillation frequency of an unexcited single impinging round jet (see e.g. Liu & Sullivan 1996). This analysis indicates that LCT cannot be used in this case to produce instantaneous snapshots of the temperature field as a consequence of impacting eddies on the surface or jet oscillations; only ensemble mean temperature distributions will therefore be used for the analysis of impinging jet heat transfer.

The ensemble-averaged heat transfer was calculated from 200 images for each of the 140 different combinations of the experimental parameters. The uncertainty of the jet heat transfer coefficient calculated using the method of Kline & McClintock (1953) was about 2 % on average. In some cases, the calibrated temperature range of the liquid crystals was exceeded, causing the measured temperature to be undefined. On average, this occurred at 6.4 % of all points. The probability of undefined temperatures is highest in the region outside the impingement zone for low H/D_m values, low s/D_m, and low Reynolds numbers. These undefined points were excluded from the calculation of mean values of the Nusselt number by substituting zero for the Nusselt number at these points:

$$\langle Nu(x, y)\rangle = \frac{\sum_{i=1}^{N} Nu(x, y)_i}{N - n_{undef}(x, y)}, \tag{2.2}$$

where $\langle Nu(x, y)\rangle$ is the ensemble-averaged Nusselt number on the position (x, y), N is the total number of images in the ensemble (200), $Nu(x, y)_i$ is the Nusselt number at (x, y) from image i, and $n_{undef}(x, y)$ is the number of undefined temperatures at (x, y) in the ensemble.

2.4. *Flow measurement system*

The PIV system (manufactured by Optical Flow Systems, OFS) included a double-pulsed Nd:YAG laser (Continuum Minilite) with a pulse energy of 25 mJ. This laser was used to produce a 1 mm thick sheet that illuminated the flow. A PCO Sensicam camera with a resolution of 1280×1024 pixels recorded images of the seeding particles in the laser sheet. The commercial software VidPIV Rowan v4.0 developed by OFS/ILA was used to analyse the images. The seeding consisted of an aqueous glycerol solution and was produced by a Laskin nozzle. The laser produced a light sheet perpendicular to the impingement plate and the orifice plate and the camera recorded images of particles in the light sheet from the side. Table 2 presents the recording parameters of the PIV system for the two different configurations, together with the dynamic ranges for all flow measurements (see also Geers, Tummers & Hanjalić 2004).

2.5. *Flow measurements and data analysis*

In the hexagonal orifice configuration with $s/D_m = 2$, PIV measurements were carried out in two planes parallel to the jets (planes 1 and 3), marked in figure 2(*a*). Plane 1 intersects the central jet and one of its direct neighbours, and plane 3 intersects the central jet and one of the outer jets. The origin of a x,y,z-coordinate system is at the intersection of the centreline of the central jet and the surface of the impingement plate. The y-axis is measured along this centreline and assumed to be positive in the upward direction. The x- and z-axes are measured along the surface of the impingement plate. The measurement area was defined by $-4.4 < x/D_m < 1.0$ and $0.0 < y/D_m < 4.0$ for both planes in the hexagonal configuration.

In the in-line orifice configuration with $s/D_m = 4$, we performed PIV measurements in three vertical planes (planes *a*, *b*, and *c*) depicted in figure 2(*b*). Plane *a* intersects the central jet and one of its direct neighbours, plane *b* intersects the central jet and one of the outer jets and plane *c* intersects one of the central jet's direct neighbours and one of the outer jets. The measurement area was defined by $-1.2 < x/D_m < 5.0$ and $0.0 < y/D_m < 4.0$ for planes *a* and *c*, and $-0.7 < x/D_m < 6.6$ and $0.0 < y/D_m < 4.0$ for plane *b*. Additionally, measurements were carried out in one horizontal plane in

	Hexagonal jet array	In-line jet array	
	Vertical	Horizontal	Vertical
Focal length lens (mm)	105	55	55
Numerical aperture	11	8	8
Field of view (mm^2)	71.2×52.0	85.2×66.2	75.5×52.0
Interrogation area size (px)	32×32	64×64	32×32
(mm^2)	1.8×1.8	4.7×4.7	2.0×2.0†
			2.4×2.4‡
Particle image size (px)	2.3	1.7	1.7
Interrogation area overlap (%)	50	50	50
Pulse delay (μs)	20.0	6.0	21.8 †
			25.8 ‡
Dynamic velocity range (m s^{-1})	0.28 : 22	0.73 : 116	0.29 : 23
		1.2 : 198	
Reynolds number	1.8×10^4	2.0×10^4	2.0×10^4
Number of snapshots	3000	3000	3000

†planes *a* and *c*
‡plane *b*

TABLE 2. PIV recording parameters for all experiments.

the in-line configuration at $0.54D_m$ above the impingement plate. This was done by creating a light sheet parallel to the impingement plate, positioning the PIV camera under the impingement plate, which in this case was made of glass. The horizontal plane focuses on the same four jets: the central jet, two of its direct neighbours and one of the outer jets. The position of the measurement area was $-1.9 < x/D_m < 5.3$ and $-0.8 < z/D_m < 5.0$.

The images resulting from all configurations were analysed in three consecutive steps. First, the interrogation areas were cross-correlated and a local median filter was used to discard the spurious vectors. The resulting empty spaces were filled with interpolated values from the surrounding interrogation areas. The resulting displacement fields were used as window displacements for an adaptive cross-correlation of the same interrogation areas in the second step. After filtering out and replacing the spurious vectors, the second step is repeated. The percentage of spurious vectors was 4 % on average for all vertical planes and about 3 % for the horizontal plane. The motivation for repeating the second step is a significant reduction of the number of spurious vectors.

Dominant flow structures can be defined and extracted from turbulent flow fields on the basis of the proper orthogonal theorem of probability (Loève 1955), as proposed by Lumley (1967). Proper orthogonal decomposition (POD) provides an optimal set of basis functions for an ensemble of data. It is optimal in the sense that it is the most efficient way of extracting the most energetic components of an infinite dimensional process with only a few modes (Holmes, Lumley & Berkooz 1996). When applied to experimental data, the POD can be viewed as a filtering device used to objectively eliminate the low-energy motions of the flow that are obscuring the main energetic features of the flow (Gamard *et al.* 2002).

From the PIV data in each plane, an ensemble of 1000 images was taken to determine the POD at that plane. Next, the snapshots in this ensemble were reconstructed using the 21 most energetic modes (including mode 0, which represents

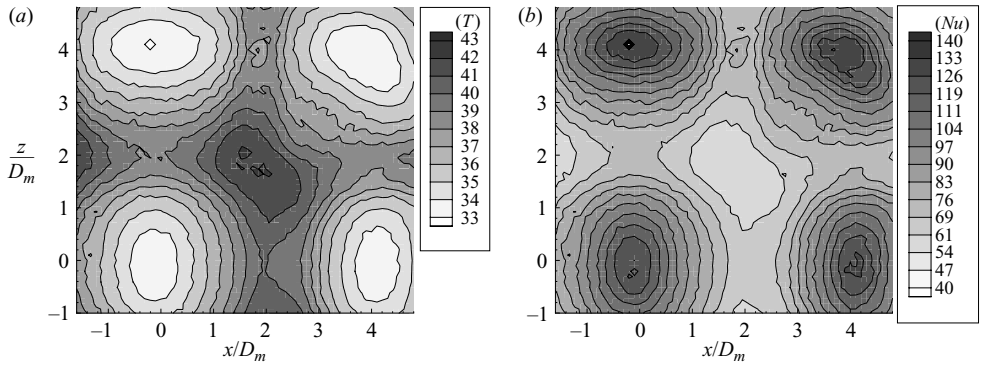

FIGURE 7. Example of the mean temperature distribution of the in-line configuration with $s/D_m = 4$, $H/D_m = 4$, and $Re = 2.0 \times 10^4$. (*a*) Mean surface temperature; (*b*) mean heat transfer.

the ensemble mean flow field). In this way, high-frequency fluctuations were filtered out, while the inhomogeneity of the flow field remained intact.

3. Results

3.1. *Local heat transfer: in-line configuration*

In figure 7, a typical surface temperature distribution is presented together with the corresponding Nusselt number distribution for the in-line configuration with $s/D_m = 4.0$ and $H/D_m = 4.0$, at $Re = 2.0 \times 10^4$. In the impingement regions of the four jets the temperature is lowest, about 33 °C, owing to the efficient cooling effect of jet impingement. This corresponds to the highest Nusselt number, about 140. In between the impingement regions, the temperature can increase up to a maximum of 43 °C, which is approximately 10 K higher than in the impingement regions and gives rise to a relatively low Nusselt number of about 40. This is mainly due to the decrease of the radial wall jet velocity with increasing distance from the jet impingement point and the heating of the air in the wall jet. Because the Nusselt number is inversely proportional to the temperature difference between the impingement surface and the fluid in the jets, the mean heat transfer distribution is very similar to the mean temperature distribution.

The impingement zones of the neighbouring jets at $(x/D_m, z/D_m) = (4.0, 0.0)$ and (0.0, 4.0) appear to be oval. This phenomenon can be clarified by investigating the flow field of the neighbour jets. In figure 8(*a–c*) the mean flow field and the distribution of turbulence kinetic energy k are presented in all three vertical planes in the in-line configuration. In these plots, k is estimated from the two-component PIV data as $(2\langle u'^2\rangle + \langle v'^2\rangle)/2$, where $\langle u'^2\rangle$ and $\langle v'^2\rangle$ are the mean square values of the two measured components of velocity fluctuations in the x- and y-directions, respectively. It was assumed that the magnitude of the (out-of-plane) third velocity component $\langle w'^2\rangle$ was comparable to that of $\langle u'^2\rangle$. Only a quarter of the total number of vectors is shown for reasons of clarity. A clear distortion of the jet at $x/D_m = 4.0$ can be seen in figure 8(*a*). The 'inner' edge of the jet at $x/D_m \approx 3.5$ is deflected outwards, while the 'outer' edge at $x/D_m \approx 4.5$ is perpendicular to the impingement wall. The cross-section of the jet seems to become smaller. This phenomenon appears clearly in figure 9, in which profiles are presented of the wall-normal velocity component at different heights above the impingement plate.

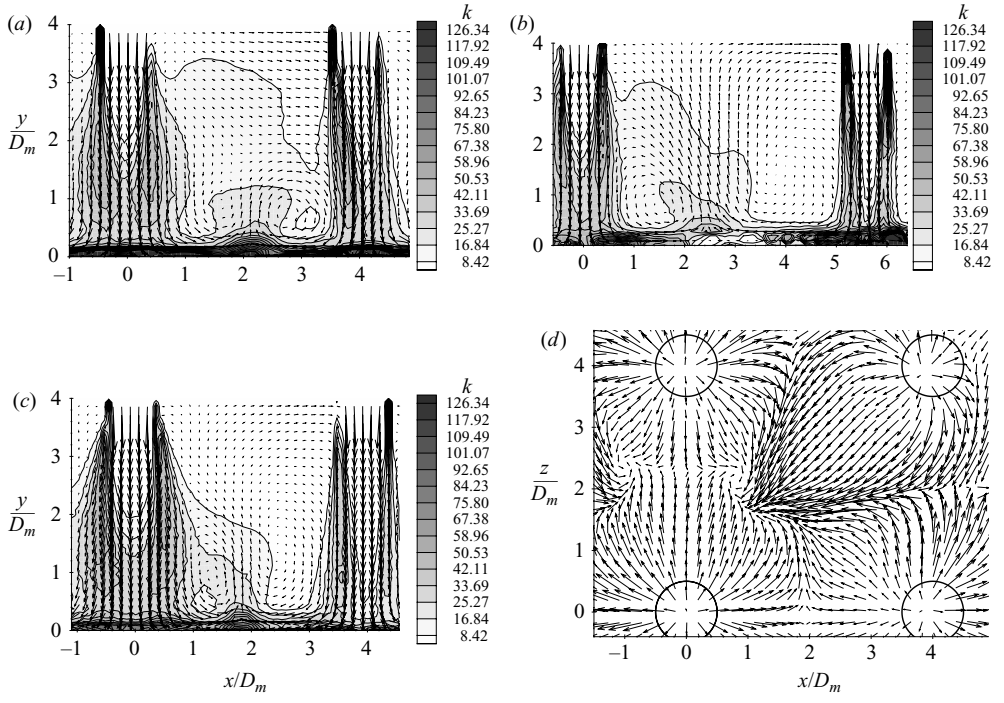

FIGURE 8. Mean velocity and k distributions in the three vertical planes and mean velocity distribution in the horizontal plane for the in-line array with $s/D_m = 4$, $H/D_m = 4$, and $Re = 2.0 \times 10^4$. (*a*) Vertical plane *a*; (*b*) vertical plane *b*; (*c*) vertical plane *c*; (*d*) horizontal plane at $y = 0.54D_m$.

The wall-parallel distance to the centre jet x was non-dimensionalized by the jet diameter, D_m, and the velocity was non-dimensionalized by the centreline exit velocity of the centre jet, U_{CL}. As can be seen in figure 9, the centre jet (at $x/D_m = 0.0$) is increasing in width, while the width of the neighbouring jet (at $x/D_m = 4.0$) is decreasing. Note that the profiles of the two jets are similar in shape and have comparable maxima. Hence, for mass conservation in the neighbouring jet, this jet must become wider in the out-of-plane direction and assume an ellipsoidal shape as it approaches the impingement plate. A clarifying sketch is presented in figure 10, where the dashed lines show the disturbed impingement patterns.

Contrary to what was expected, the centre jet also produces an oval heat transfer pattern. It is likely that this effect is caused by an asymmetrical flow field. Figure 8(*d*) shows the mean velocity distribution in the horizontal plane at $0.54D_m$ above the impingement plate of the in-line configuration. There appears to be no symmetry around the diagonal line $x = z$. In the upper left-hand region, the flow exhibits a local vortical pattern centred at x/D_m, $z/D_m \approx 0.9, 2.3$. On the basis of geometrical symmetry of the orifice plate in the diagonal $x = z$, it is highly likely that the vortex also occurs on the other side of the diagonal. In fact, from studying 150 individual snapshots randomly picked from the ensemble, a clear vortex was found above the diagonal in 20 % of the snapshots and below the diagonal in 10 % of the snapshots, while no clear evidence of a vortex was found in the remaining 70 %. In other words, the vortex can occur at both positions, but there is a preference for the vortex to be above the diagonal. It is unlikely that the vortex is caused by some

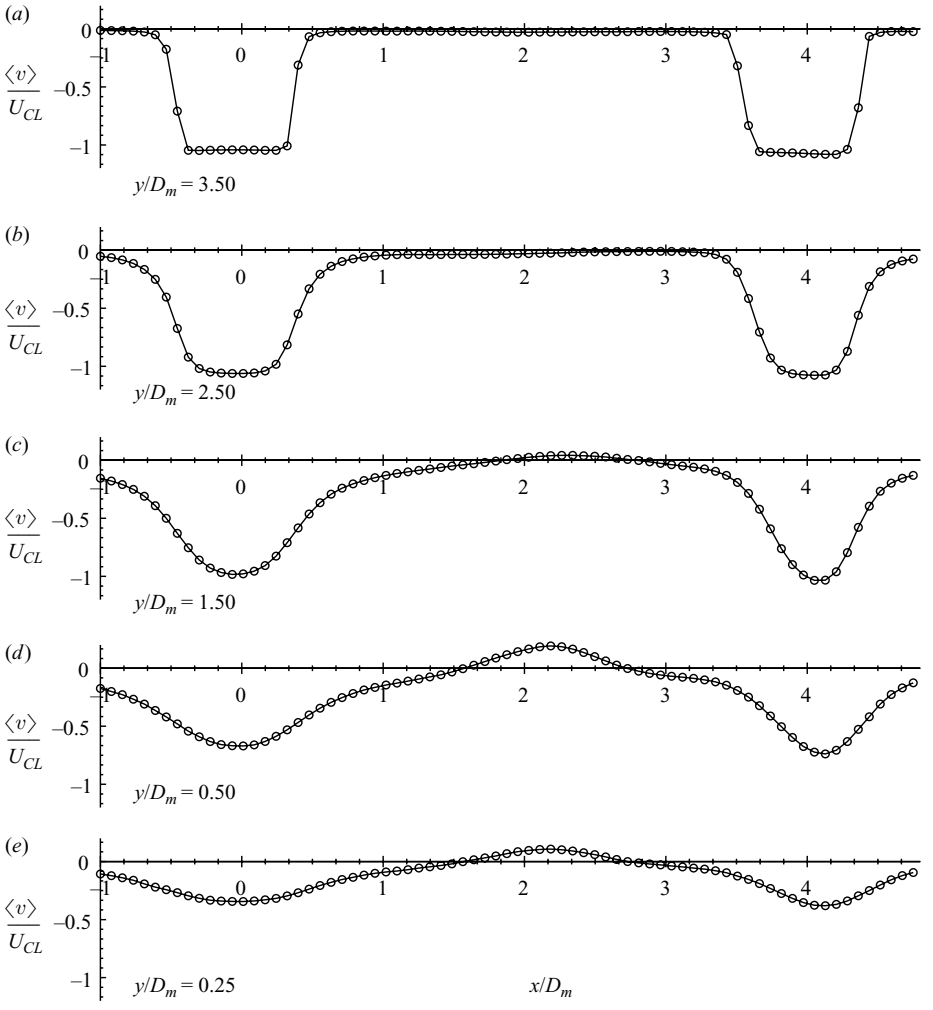

FIGURE 9. Profiles of $\langle v \rangle / U_{CL}$ at different heights above the impingement plate for the in-line array.

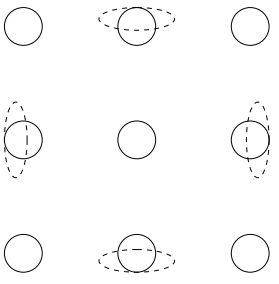

FIGURE 10. Sketch of the neighbouring jet distortion.

imperfection of the experimental set-up (e.g. scratches or burrs on the edges of the orifice) that would break the symmetry. The fact that the vortex is occurring at (−0.9, 2.3) substantiates the conclusion that this is not a consequence of experimental

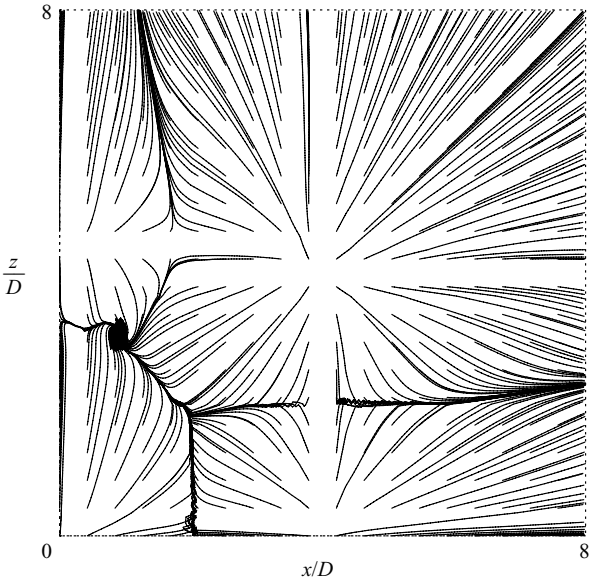

FIGURE 11. Path lines in a horizontal plane at $0.01D_m$ above the impingement plate for the in-line configuration resulting from numerical simulations (Thielen *et al.* 2003).

imperfection, but a physical phenomenon. However, the intensity of the vortex is weak compared to the impinging jets, and hence its location can be sensitive to external disturbances. Possibly the preferential position of the vortex is determined by obstacles in the far field of the flow (i.e. beyond the measurement zone). It is noted that the numerical computations by Thielen, Jonker & Hanjalić (2003) also showed the existence of such a vortex. Figure 11 presents path lines in a horizontal plane $0.01D_m$ above the impingement plate for the in-line configuration resulting from these numerical calculations. At first, this was thought to be a numerical artefact, because no experimental data were available for the in-line configuration at the time of discovery. For this reason, special care was taken to ensure that the asymmetry did not have a numerical origin. The computations were checked on their dependence of the grid, the differencing scheme used, the initial conditions, the fact that the calculations were steady or unsteady, and the computer code used to calculate the flow field. Because in numerical simulations ideally symmetric boundary and inflow conditions are imposed, the appearance of the asymmetry suggests that this is a genuine phenomenon and that it is not caused by experimental deficiencies. Its cause is probably the natural asymmetry and possible local bifurcation pertinent to this particular (in-line) orifice configuration with relatively large pitch: a low-momentum circulation region is created and trapped in either the upper or lower corner. It is noted that the appearance of asymmetric flows in symmetric geometries is not uncommon. For instance, Roksnoer *et al.* (1989) and van Santen, Kleijn & van den Akker (2000) show that symmetry breaking also appears in VPE and CVD reactors.

3.2. *Local heat transfer: hexagonal configuration*

Contour plots of mean heat transfer results for the hexagonal array with sharp-edged orifices are presented in figure 12 for two values of the pitch ($s/D_m = 2$ and 6) and two orifice-to-plate distances ($H/D_m = 4$ and 10) at a Reynolds number of 2.0×10^4.

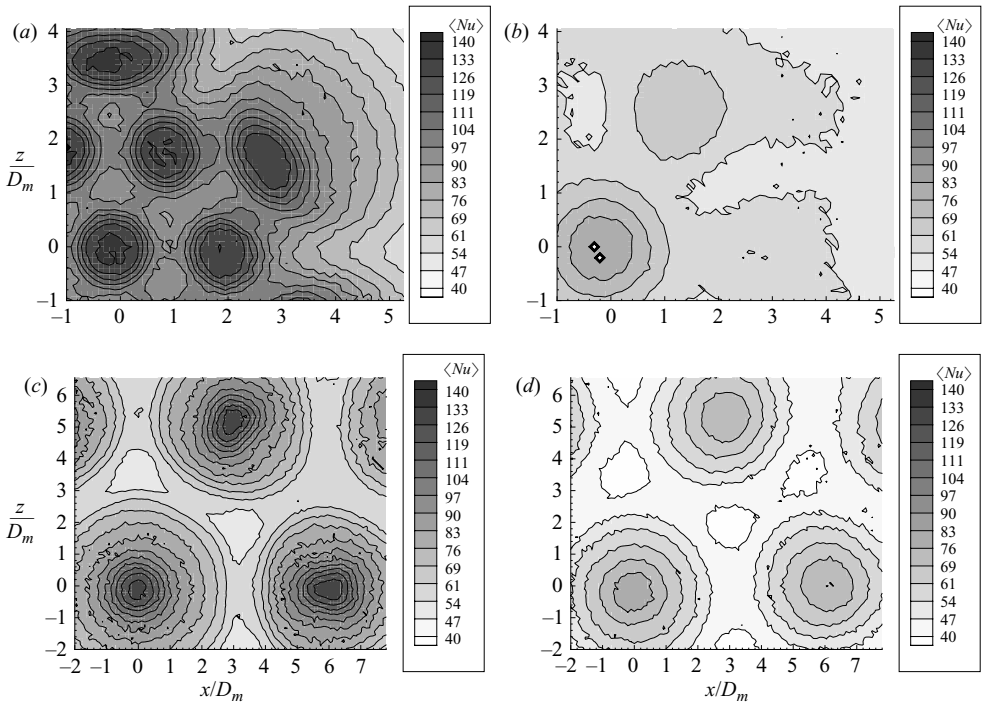

FIGURE 12. Ensemble-averaged Nusselt numbers for four configurations of the hexagonal array with sharp-edged orifices at $Re = 2.0 \times 10^4$. (*a*) $s/D_m = 2$, $H/D_m = 4$; (*b*) $s/D_m = 2$, $H/D_m = 10$; (*c*) $s/D_m = 6$, $H/D_m = 4$; (*d*) $s/D_m = 6$, $H/D_m = 10$.

In figure 12(*a*), the impingement pattern of the jets can be seen clearly, whereas at higher orifice-to-plate distance this pattern appears to deteriorate owing to the strong jet–jet interaction. Note that the two white spots near (0,0) in figure 12(*b*) are caused by erroneous values. At $H/D_m = 10$, the individual jets have lost their identity owing to mixing by the large-scale structures in the flow. In case of a larger pitch ($s/D_m = 6$, figure 12*c*, *d*) the distortion of the jets is less, and the impingement pattern can still be discerned at $H/D_m = 10$. Figure 13 shows two reconstructed snapshots for each of the planes 1 and 3 in the hexagonal arrangement on the basis of 21 POD modes. In all figures, the jets can be discerned clearly. They appear to be largely unaffected down to $y/D_m = 2$, but below this position the jets are disturbed by eddies originating from the interaction of the jets with the impingement surface. For instance, in figure 13(*b*) the centre jet is either broken up or severely displaced out-of-plane. This explains the rising levels of k and the strong deceleration of the jet velocity in the centrelines of the jets, which causes a deterioration of the heat transfer in the impingement regions. With growing orifice-to-plate distance, this deterioration becomes stronger.

To further support the evidence of the loss of identity below $y/D_m = 2$, figure 14 presents the size distribution of all eddies identified in the POD ensemble of vertical plane 3. Each dot represents an eddy. Figure 14(*a*) shows all eddies in a size range between $0.1D_m$ and $0.2D_m$, and figure 14(*b*) shows all eddies between $0.2D_m$ and $0.3D_m$ in size. The eddies were identified on the basis of the second invariant of the velocity gradient tensor Q exceeding the threshold level of $1.0U_{CL}^2/D_m^2$. The characteristic diameter D_e of an eddy was calculated on the basis of the total area A enclosed by

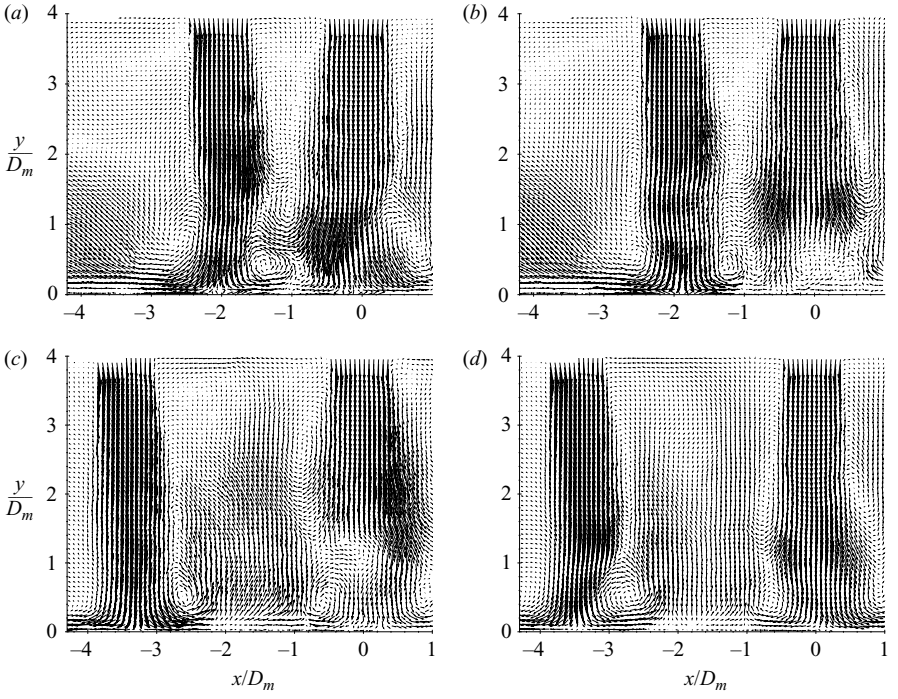

FIGURE 13. POD filtered snapshots (mean field and the first 20 modes) in vertical planes 1 and 3 of the hexagonal arrangement with $s/D_m = 2$, $H/D_m = 4$ and $Re = 2.0 \times 10^4$. (*a*) Snapshot 1 in plane 1; (*b*) snapshot 2 in plane 1; (*c*) snapshot 1 in plane 3; (*d*) snapshot 2 in plane 3.

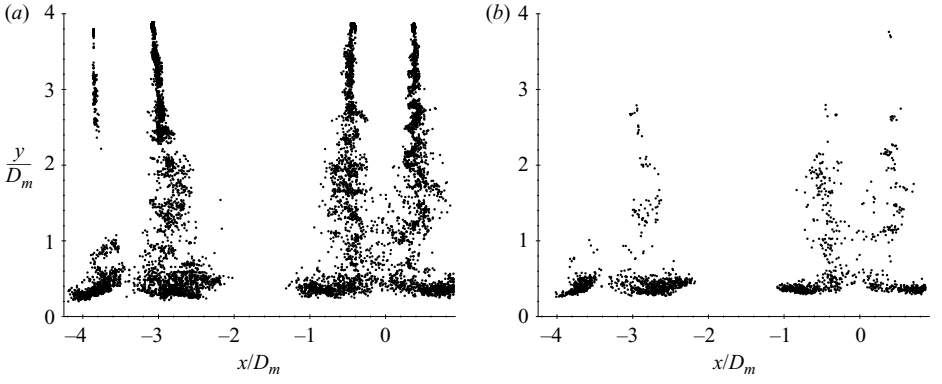

FIGURE 14. Size distribution of eddies located in vertical plane 3 of the hexagonal configuration with sharp-edged orifices. (*a*) $0.1 < D_e/D_m \leqslant 0.2$; (*b*) $0.2 < D_e/D_m \leqslant 0.3$.

the eddy:

$$D_e = \sqrt{\iint_A \mathrm{d}x\,\mathrm{d}y}. \tag{3.1}$$

In figure 14(*a*), the impinging jets are clearly visible by the eddies in the shear layers and near the impingement centre points. In the downstream direction of the jets, the spreading of the shear layers is clearly shown by the broadening of the regions of eddies. Figure 14(*b*) shows that the eddies are growing in the downstream direction, as

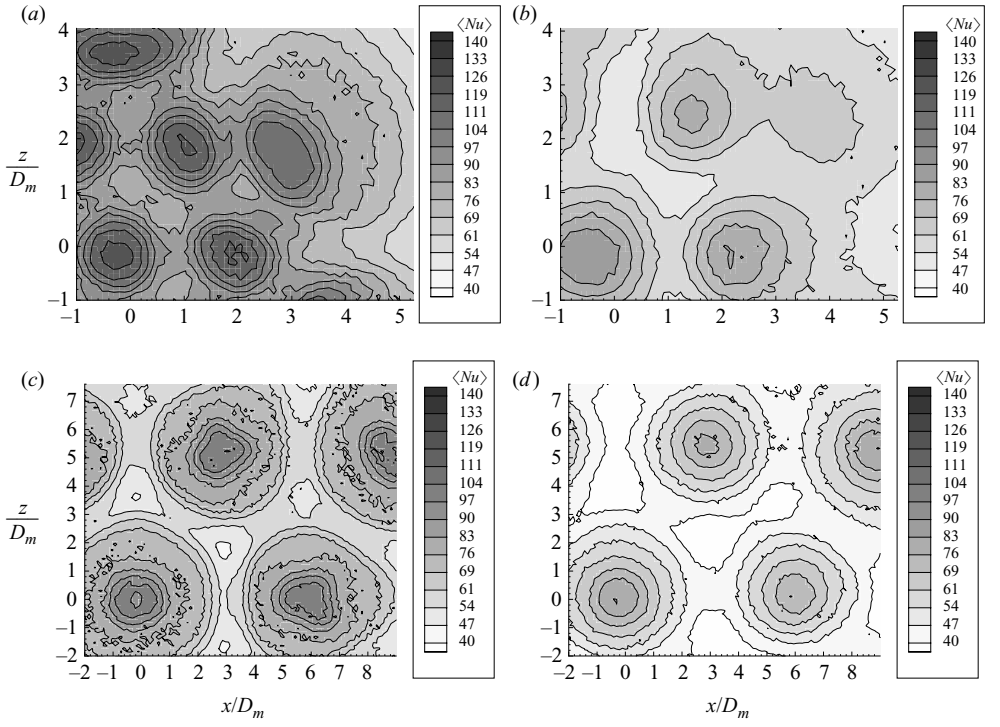

FIGURE 15. Ensemble-averaged Nusselt numbers for four configurations of the hexagonal array with contoured orifices at $Re = 2.0 \times 10^4$. (*a*) $s/D_m = 2$, $H/D_m = 4$; (*b*) $s/D_m = 2$, $H/D_m = 10$; (*c*) $s/D_m = 6$, $H/D_m = 4$; (*d*) $s/D_m = 6$, $H/D_m = 10$.

their density increases. It is clear that eddies in this size range appear most frequently below $y/D_m = 2$, where they strongly affect the jets and cause them to meander or break up and thus lose their identity.

The investigation of the heat transfer in the hexagonal array with contoured orifices yields similar results. Figure 15 presents these results for the same values of s/D_m, H/D_m and Re as for the hexagonal array with sharp orifices shown above. At $H/D_m = 4$ the heat transfer in the impingement points is higher for the sharp-edged orifices than for the contoured orifices. This is because the jets emerging from the sharp-edged orifices have a higher initial velocity owing to the vena contracta. In case of the contoured orifices the vena contracta effect is much smaller or maybe even absent. At $H/D_m = 10$ the differences in heat transfer are much smaller.

Figure 16 shows profiles of the Nusselt number along a line through the centre jet and one of its direct neighbours as a function of H/D_m at $Re = 2.0 \times 10^4$ for both hexagonal configurations. The results are given for the sharp-edged orifices (figure 16*a*, *c*, *e*) and the contoured orifices (figure 16*b*, *d*, *f*) for three values of the pitch. In all cases, the Nusselt number is decreasing with increasing orifice-to-plate distance, because the jet centreline velocity decreases owing to entrainment and jet-jet interaction.

In figure 16(*a*), the impingement pattern of the neighbouring jet at $x/D_m = 2.0$ has nearly vanished for $H/D_m = 10.0$. This is most probably caused by a combination of jet–jet interaction prior to impingement and crossflow induced by the outflow of spent air from the centre jet. Both these effects are particularly strong at small

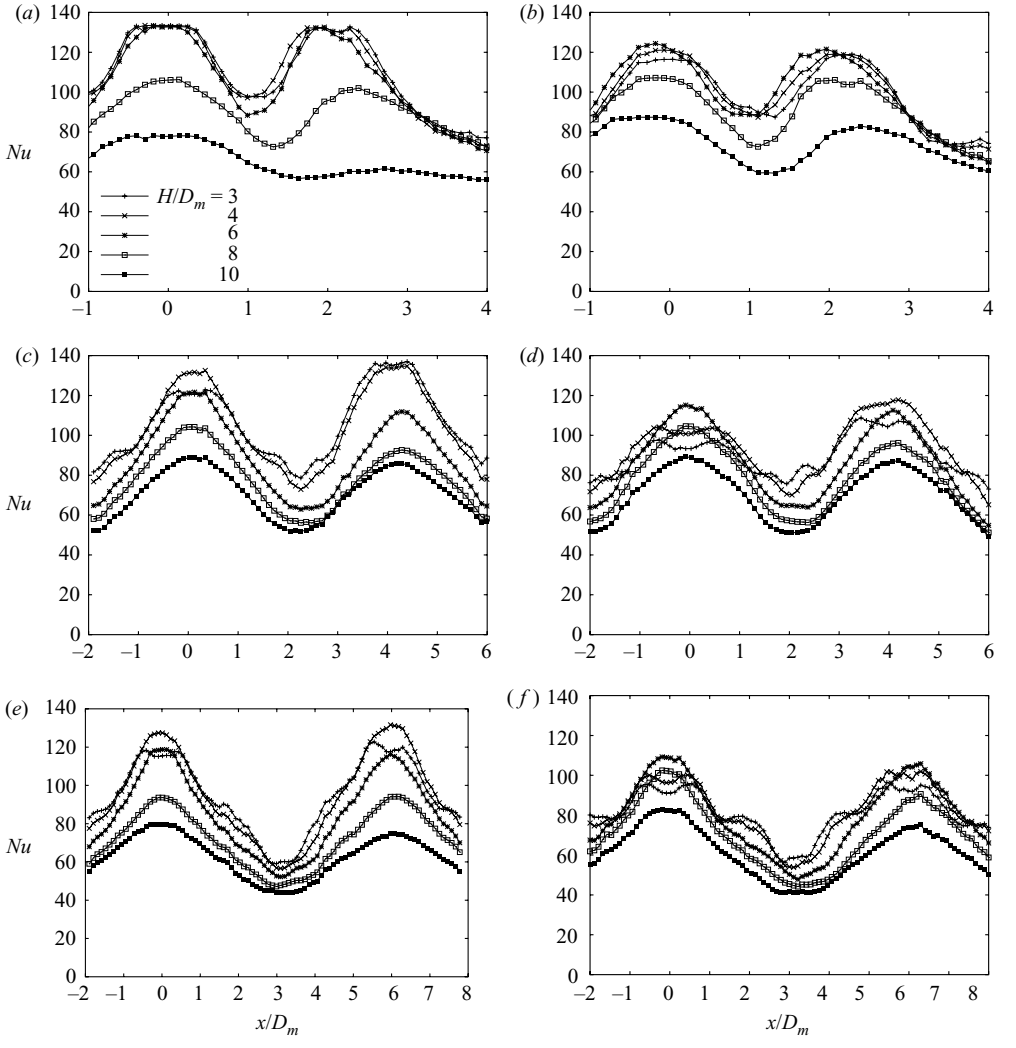

FIGURE 16. Profiles of the local Nusselt number for all hexagonal configurations at $Re = 2.0 \times 10^4$. Sharp-edged orifices: (*a*) $s/D_m = 2$, (*c*) $s/D_m = 4$, (*e*) $s/D_m = 6$; contoured orifices: (*b*) $s/D_m = 2$, (*d*) $s/D_m = 4$, (*f*) $s/D_m = 6$.

values of the pitch. Additionally, spent air is already heated before it mixes with fresh air from neighbouring jets, explaining the lower peak Nusselt number for the neighbouring jet. Figure 16(*b*) shows a different profile for the contoured orifice plate. The impingement pattern of the jet at $x/D_m = 2.0$ is still clearly visible. Because the potential core of jets issuing from a sharp-edged orifice is shorter than for jets from a contoured orifice, interaction with neighbouring jets affects the flow more strongly in the case of the sharp-edged orifice.

A feature in figures 16(*a*) and 16(*b*) is the apparent outward displacement of the neighbouring jet at $x/D_m = 2.0$. The magnitude and trend of this displacement can be judged better by investigating the distance between the peak Nusselt numbers (that is, assuming the peak Nusselt numbers correspond to the impingement centres of the jets). In figure 17, the non-dimensional distance between the Nusselt number

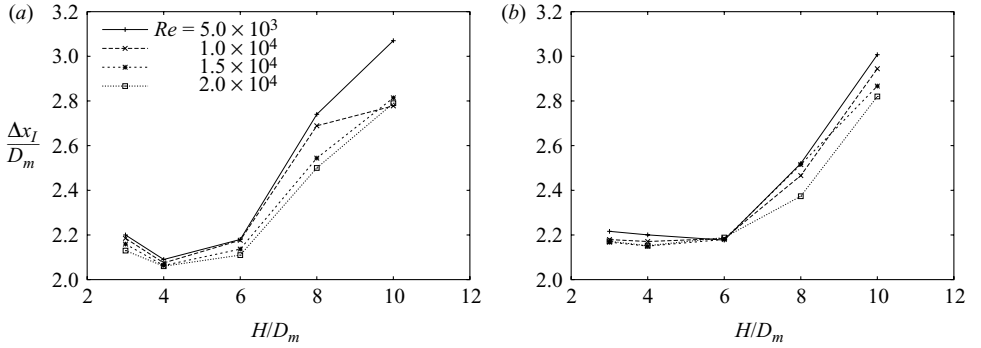

FIGURE 17. Distance between the peaks in the Nusselt number profiles for both hexagonal configurations at $s/D_m = 2.0$. (*a*) Sharp-edged orifices; (*b*) contoured orifices.

peaks $\Delta x_I/D_m$ is plotted versus the orifice-to-plate spacing for both hexagonal configurations at $s/D_m = 2.0$. The positions of the peaks were found by fitting Gaussian functions to the Nusselt number profiles shown in figures 16(*a*) and 16(*b*). A small but noticeable displacement exists already for $H/D_m \leqslant 6.0$: the peaks are a distance of about 2.1–$2.2D_m$ apart, instead of the geometric pitch of $2D_m$. This is due to the strong crossflow through the narrow space between the orifice plate and the impingement plate (Goldstein & Timmers 1982). There is a strong increase in the displacement of the outer jet when the orifice-to-plate distance is increased beyond the potential core of the jet. Possible causes for the displacement are the collision of wall jets emerging from the jet impingement zones, and the outflow of spent air from the centre jet forming a crossflow that interacts with neighbouring jets.

Finally, note the occurrence of local minima and maxima at $x/D_m \approx 2.0$ and $x/D_m \approx 4.0$ in figure 16(*f*), and to a lesser extent, in figure 16(*e*). These minima and maxima only occur at small orifice-to-plate spacings, say $H/D_m \leqslant 4$. Gardon & Cobonpue (1962) conjectured a transition from laminar to turbulent flow to be the cause of the humps. Following this conjecture, it can be stated that the laminar–turbulent transition is clearer for the contoured orifice jets, because they have a longer potential core than the sharp orifice jets. For low orifice-to-plate spacings the impingement plate is placed well into the potential core of the contoured orifice jet, but it is already at or beyond the end of the core of the sharp-edged orifice jet. Popiel & Boguslawski (1986) confirm these conclusions.

3.3. *Stagnation-point heat transfer*

The Nusselt number in the stagnation point of the central jet Nu_{stag} for all configurations and Reynolds numbers is presented in figures 18 and 19. Figures 18(*a*), 18(*c*) and 18(*e*) show the data for the hexagonal plate with sharp-edged orifices for $s/D_m = 2$, 4 and 6, respectively. For the same values of s/D_m, figures 18(*b*), 18(*d*) and 18(*f*) show the data for the hexagonal plate with contoured orifices. The data for the in-line configuration is shown in figure 19. For all configurations the stagnation Nusselt number is multiplied by the Reynolds number raised to a power $-\alpha_1$ to compare profiles conveniently at different Reynolds numbers with each other. The values for α_1 were calculated from a nonlinear fit to the surface-averaged heat transfer as a function of the Reynolds number.

From figure 18, it appears that the maximum value of $Nu_{stag}Re^{-\alpha_1}$ is at $H/D_m = 4$ for the sharp-edged orifices, while it is at $H/D_m = 6$ for the contoured orifices. This is explained by the fact that the potential core of a jet from a sharp-edged orifice

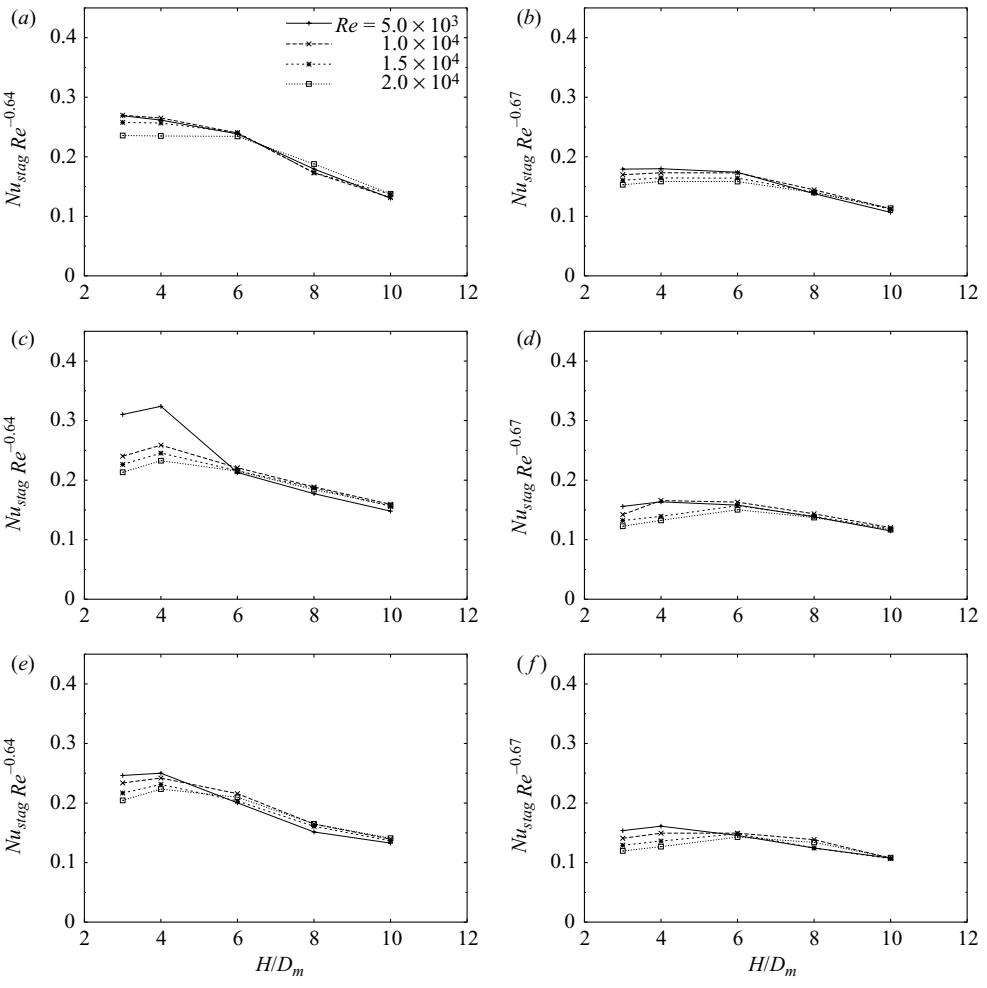

FIGURE 18. Stagnation-point Nusselt numbers for all hexagonal configurations. Sharp-edged orifices: (*a*) $s/D_m = 2$, (*c*) $s/D_m = 4$, (*e*) $s/D_m = 6$; contoured orifices: (*b*) $s/D_m = 2$, (*d*) $s/D_m = 4$, (*f*) $s/D_m = 6$.

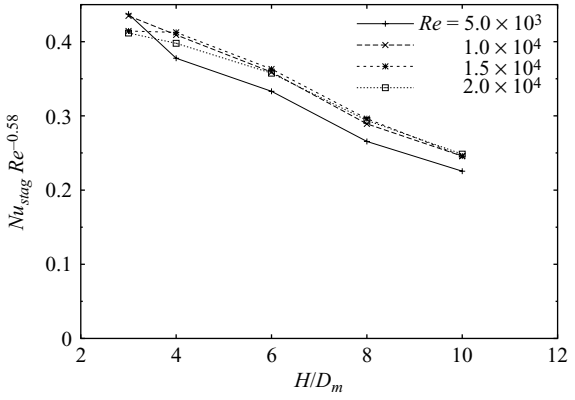

FIGURE 19. Stagnation-point Nusselt numbers for the in-line configuration.

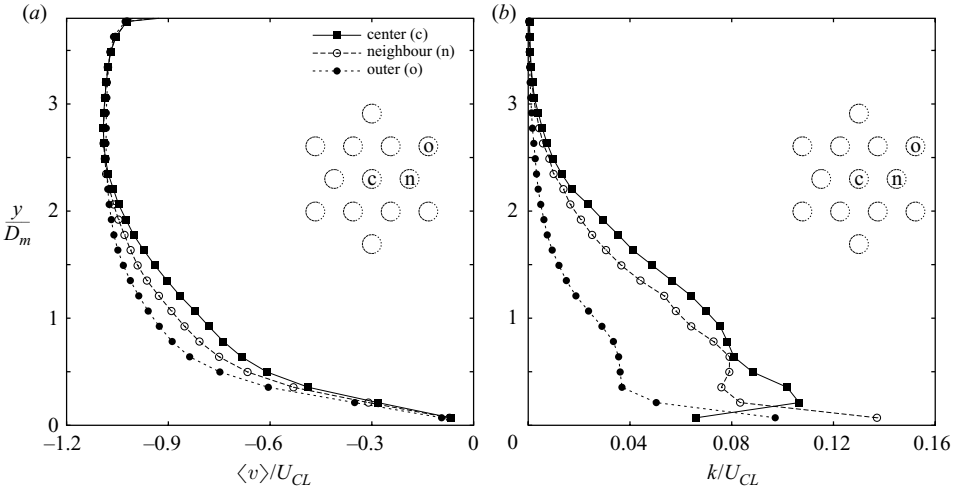

FIGURE 20. Profiles in the centrelines of the central jet, a neighbouring jet, and an outer jet in the hexagonal arrangement with sharp-edged orifices with $s/D_m = 2$, $H/D_m = 4$, and $Re = 2.0 \times 10^4$. (*a*) Mean velocities; (*b*) turbulence kinetic energy.

due to stronger edge shear is smaller than the core of a jet from a contoured orifice. Below the orifice-to-plate spacing at which $Nu_{stag}Re^{-\alpha_1}$ is maximum, the impingement plate is in the potential core region where the level of turbulence is very low and the jet is stable. At the end of the potential core, the turbulence level (defined as $\sqrt{\langle u'^2 \rangle}/U_{CL}$) rises and the centreline velocity decreases. This can be seen in figures 20(*a*) and 20(*b*), which show the mean axial velocity component $\langle v \rangle$ and the turbulence kinetic energy k as a function of the wall-normal distance y on the centrelines of the centre jet at $(x/D_m, z/D_m) = (0.0, 0.0)$, the neighbouring jet at $(x/D_m, z/D_m) = (2.0, 0.0)$, and the outer jet at $(x/D_m, z/D_m) = (3.0, \sqrt{3.0})$. The maximum stagnation-point Nusselt number is obtained in the region with high centreline velocity and maximum turbulence level (Kataoka 1990). If the impingement plate is placed even further away from the orifice plate, both the centreline velocity and the turbulence level drop significantly, which causes a drop in the heat transfer rate. Additionally, large-scale turbulence will mix spent air and fresh air, so the average temperature of the air increases and heat transfer deteriorates.

A comparison of the stagnation Nusselt numbers for the two different orifice shapes reveals that the values for the sharp-edged orifice plates are higher than those of the contoured orifice plates for low H/D_m. This is caused by the vena contracta that occurs when the flow is passed through a sharp-edged orifice (Popiel & Boguslawski 1986). This effect is negligible in the case of the contoured nozzle. Owing to this effect, the apparent orifice diameter is smaller for the sharp-edged orifices and the centreline velocity is higher at equal Reynolds numbers yielding a higher heat transfer rate in the impingement point. At high H/D_m values, the jets expand, the velocity drops, and heat transfer rates are comparable for both orifice shapes.

3.4. *Heat transfer and turbulence*

Combining the results of the flow field and heat transfer measurements, conclusions can be drawn regarding the thermal imprint of the flow field and the turbulence on the impingement plate. To this end, wall-parallel profiles are extracted from the flow field in the vertical measurement planes just above the impingement surface. These

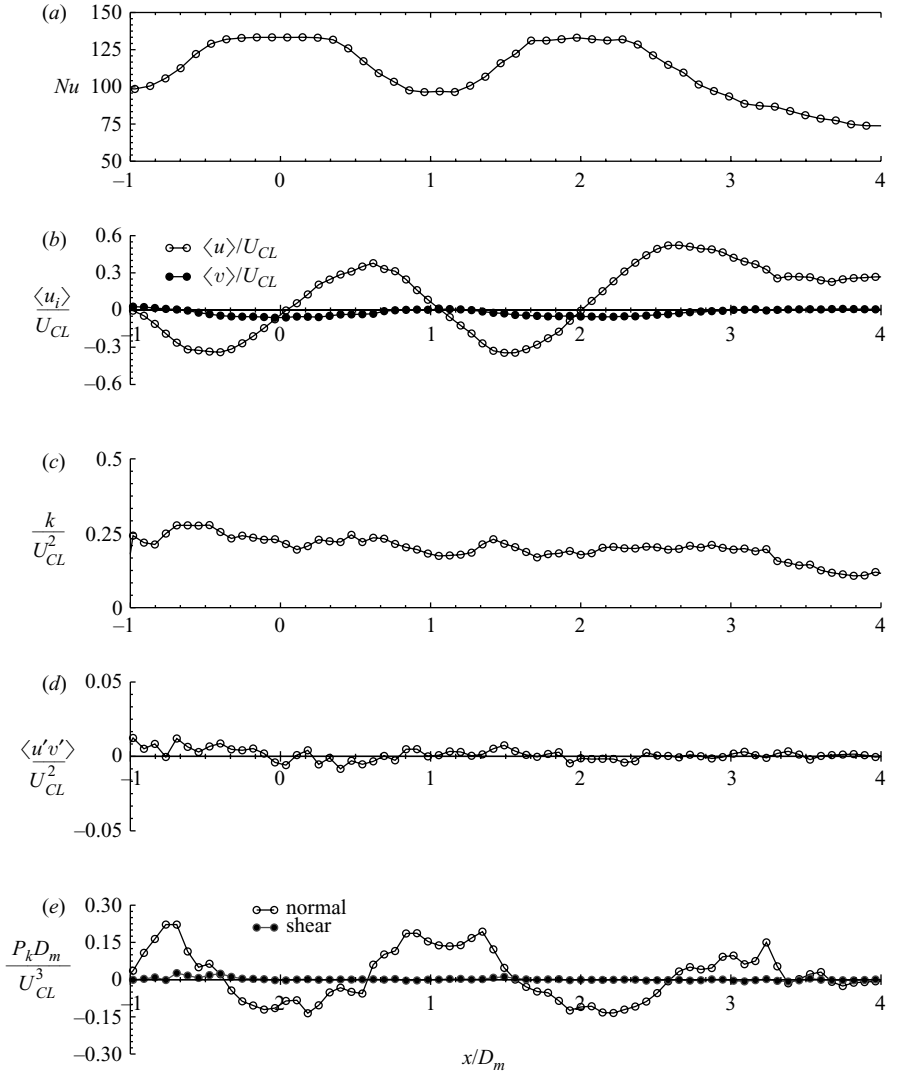

FIGURE 21. Comparison between Nu and several flow and turbulence quantities at $y = 0.07D_m$ from the wall in plane 1 of the hexagonal configuration with sharp-edged orifices, $s/D_m = 2$, $H/D_m = 4$ and $Re = 2.0 \times 10^4$.

profiles are then compared to the heat transfer on the impingement surface at the position of the planes.

In vertical plane 1 of the hexagonal sharp-orifice configuration with $s/D_m = 2$, $H/D_m = 4$, and $Re = 2.0 \times 10^4$, we have extracted profiles of the mean velocity components $\langle u \rangle$ and $\langle v \rangle$, the turbulence kinetic energy k, the turbulent shear stress $\langle u'v' \rangle$, and the normal and shear components of the production of kinetic energy P_k. Figure 21 compares these profiles with the Nusselt number measured at the intersection of plane 1 and the impingement plate. The presented flow quantities were all taken at $y = 0.07D_m$ above the impingement plate, because this is the position closest to the wall at which velocity was measured. All flow quantities are non-dimensionalized with the jet centreline velocity U_{CL} and the orifice diameter D_m.

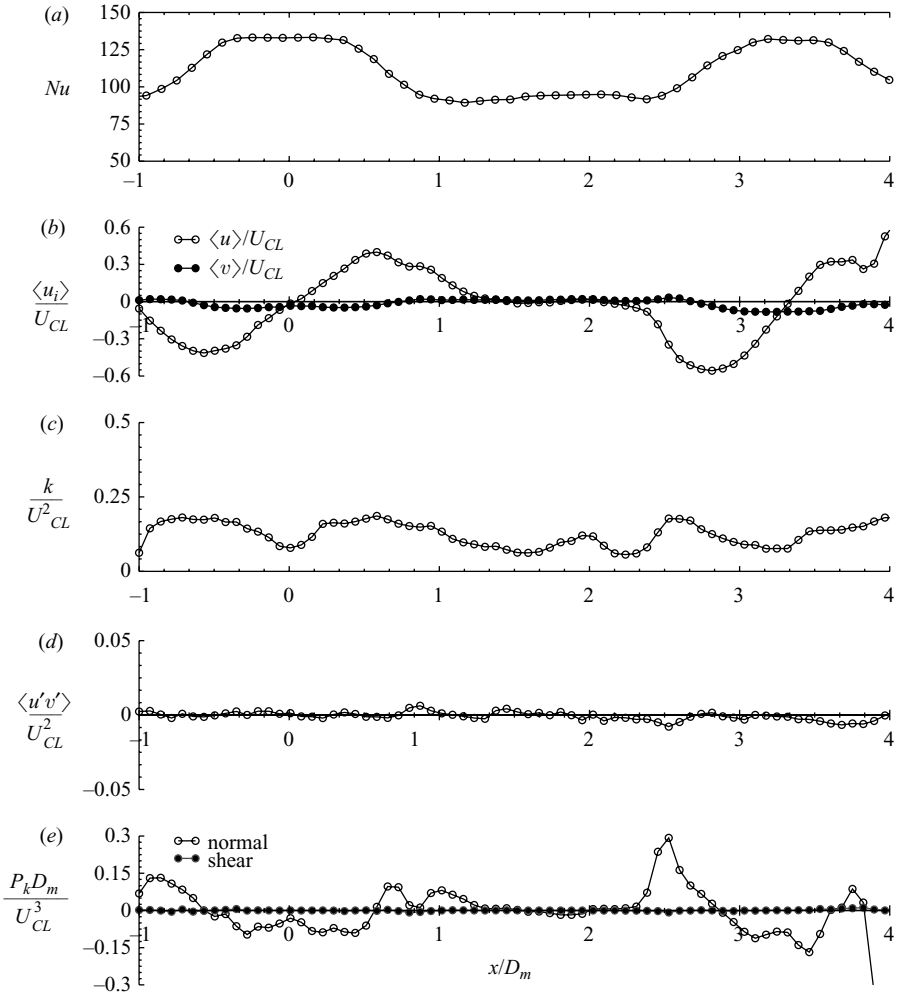

FIGURE 22. Comparison between Nu and several flow and turbulence quantities at $y = 0.07D_m$ from the wall in plane 3 of the hexagonal configuration with sharp-edged orifices, $s/D_m = 2$, $H/D_m = 4$, and $Re = 2.0 \times 10^4$.

The same quantities for vertical plane 3 in the hexagonal sharp-orifice configuration with $s/D_m = 2$, $H/D_m = 4$, and $Re = 2.0 \times 10^4$ are presented in figure 22, also acquired at $y = 0.07D_m$, whereas figures 23 and 24 show the same plots for the in-line configuration in vertical planes a and b, acquired, respectively, at $y = 0.08D_m$ and $y = 0.09D_m$ above the impingement plate for the same Re number, and with $s/D_m = 4$ and $H/D_m = 4$.

Figure 21(a) displays the Nusselt profile that has two peaks at the positions where the jets impinge on the surface. Figure 21(b) shows both components of the mean velocity. The wall-normal component $\langle v \rangle$ is very small. The wall-parallel component $\langle u \rangle$ shows very strong gradients at the impingement centre points of the jets and a net outflow at $x/D_m > 3$ forming the wall jet. The distribution of k in figure 21(c) is almost uniform and shows no clear correlation with the Nusselt number curve. The Reynolds shear stress component $\langle u'v' \rangle$ in figure 21(d) is also almost uniformly distributed and its magnitude is negligible in comparison to k. From figure 25, the

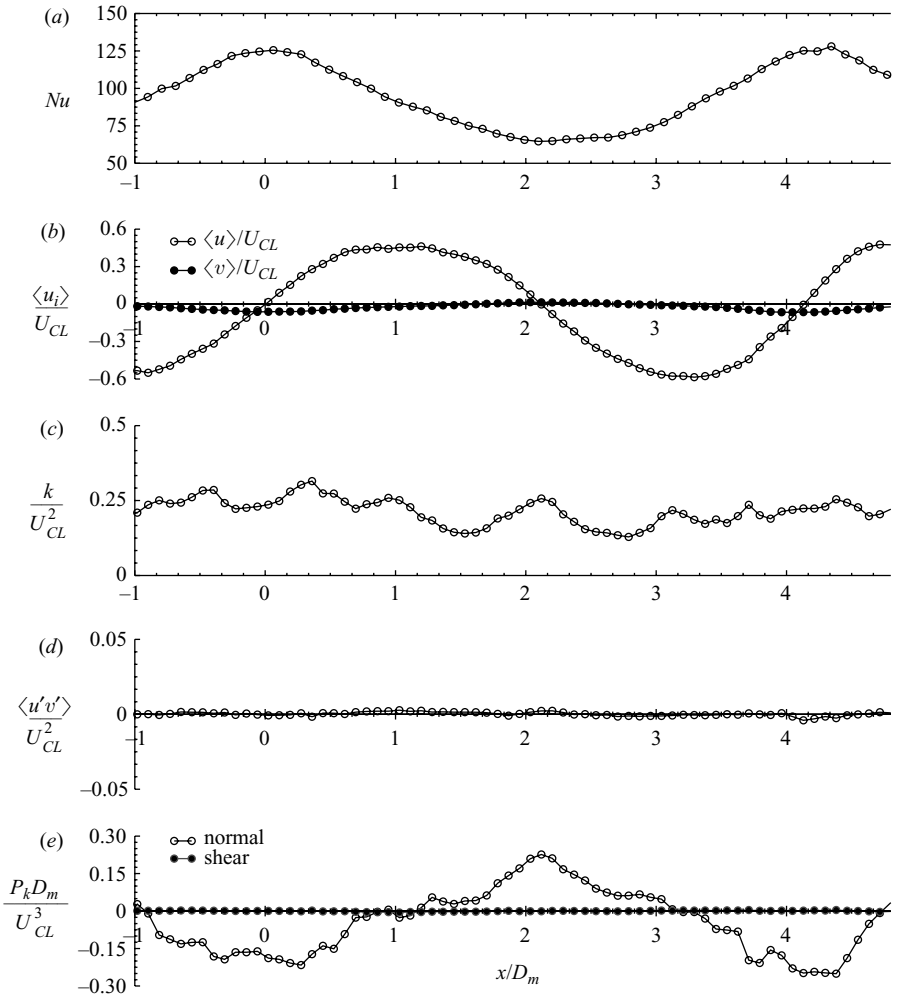

FIGURE 23. Comparison between Nu and several flow and turbulence quantities at $y = 0.08D_m$ from the wall in plane a of the in-line configuration with $s/D_m = 4$, $H/D_m = 4$, and $Re = 2.0 \times 10^4$.

wall-parallel velocity $\langle u \rangle$ appears to be at its maximum value around $y/D_m = 0.15$ for all values of x/D_m, so the gradient $\partial\langle u \rangle/\partial y$ is around zero at $y/D_m = 0.15$. According to Boussinesq's eddy-viscosity theory, $\langle u'v' \rangle$ is proportional to $\partial\langle u \rangle/\partial y + \partial\langle v \rangle/\partial x$ and as $\partial\langle v \rangle/\partial x$ is also negligible at the current position, $\langle u'v' \rangle$ will also be negligible.

Figure 21(e) shows the normal and shear components of the production of kinetic energy. These components are defined by

$$P_{k,normal} = -\langle u'^2 \rangle \frac{\partial \langle u \rangle}{\partial x} - \langle v'^2 \rangle \frac{\partial \langle v \rangle}{\partial y}, \tag{3.2}$$

$$P_{k,shear} = -\langle u'v' \rangle \left(\frac{\partial \langle u \rangle}{\partial y} + \frac{\partial \langle v \rangle}{\partial x} \right). \tag{3.3}$$

$P_{k,shear}$ is negligible compared to $P_{k,normal}$ owing to the small values of all three (right-hand) terms in (3.3). The normal production, on the other hand, is quite significant

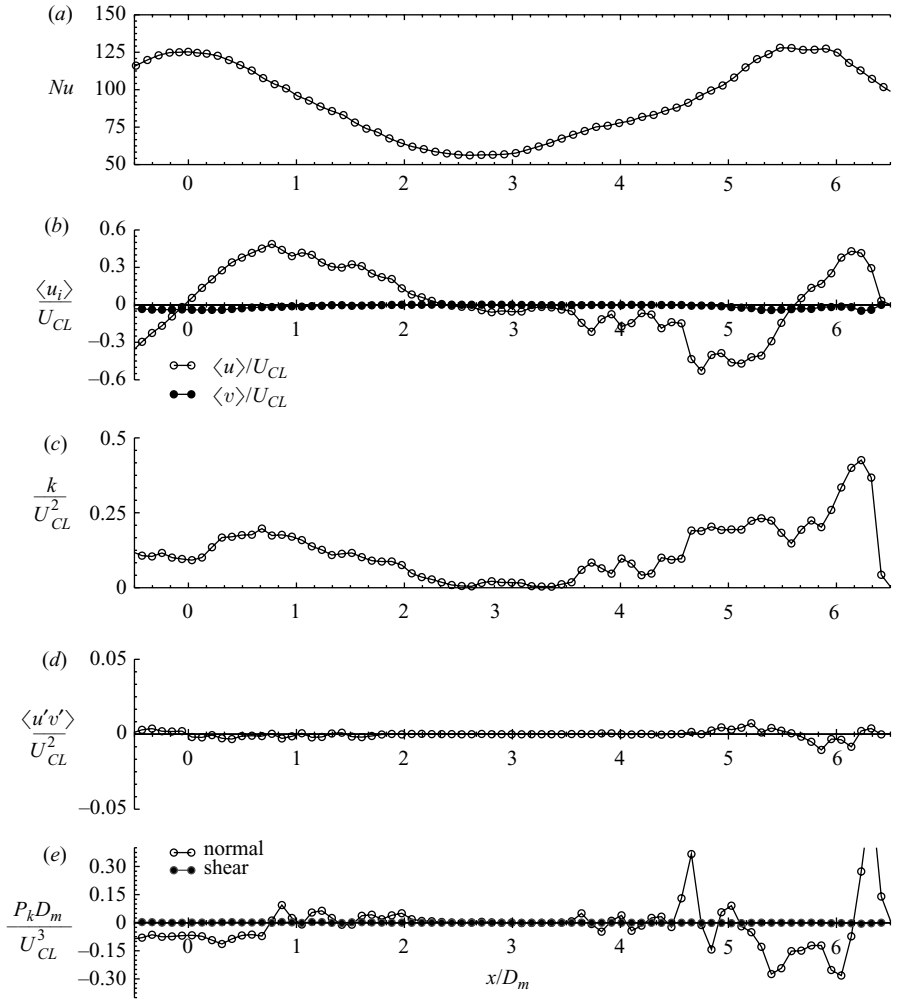

FIGURE 24. Comparison between Nu and several flow and turbulence quantities at $y = 0.09D_m$ from the wall in plane b of the in-line configuration with $s/D_m = 4$, $H/D_m = 4$, and $Re = 2.0 \times 10^4$.

but negative in the regions where the Nusselt number is high. Because $\langle u'^2 \rangle$ is the dominating contribution to k and the gradient $\partial \langle u \rangle / \partial x$ in the stagnation region is positive and much stronger than $\partial \langle v \rangle / \partial y$, the first term on the right-hand side in (3.2) is the main contribution to $P_{k,normal}$.

Comparing the production of kinetic energy with the Nusselt number, there seems to be a correlation between the negative normal production and the Nusselt number. However, this is mere coincidence: we conjecture that the major cause of the increase of Nu is a very strong acceleration of the fluid from the centre of the jet outwards, supported by the oscillation of the jet impingement centre owing to jets flapping and strong eddies penetrating into the stagnation region. Both the strong acceleration and the penetration of eddies into the boundary layer will make the boundary layer in the impingement region very thin and, consequently, impose a very steep temperature gradient, thus enabling impinging eddies to encapsulate and remove heat very efficiently. Beyond a distance of about $x \approx 0.5D_m$ from the stagnation point,

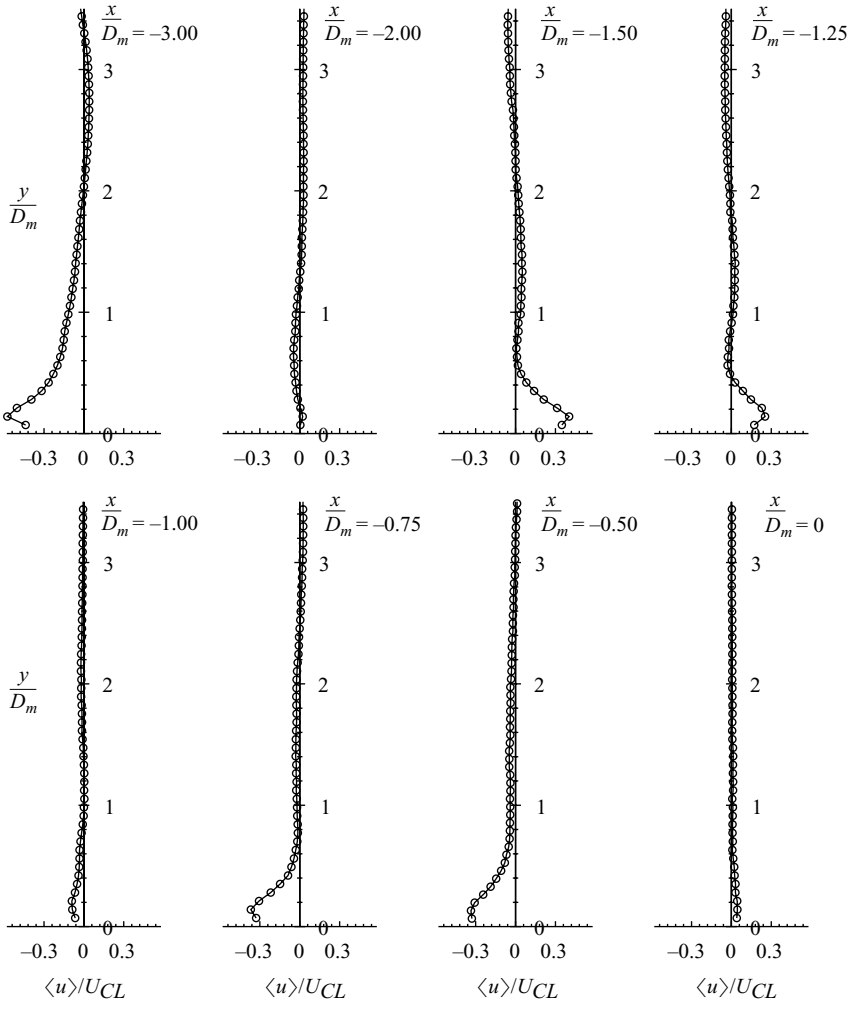

FIGURE 25. Profiles of $\langle u \rangle$ at different distances from the centre jet for the hexagonal array with sharp-edged orifices, $s/D_m = 2$, $H/D_m = 4$, and $Re = 2.0 \times 10^4$.

the fluid is decelerating and the boundary layer thickens (Colucci & Viskanta 1996), thereby reducing the heat transfer.

If the jet were laminar and the stagnation point of the jet were at a fixed position on the impingement plate, there would be a local minimum in the Nusselt number profile at the position of the stagnation point, because the velocity of the fluid in the impingement point is zero. This is also the case for a turbulent impinging jet where the impingement plate is placed inside the potential core, as was shown earlier by Gardon & Cobonpue (1962), Popiel & Boguslawski (1986), Lytle & Webb (1991) and Colucci & Viskanta (1996). If the plate is placed at or beyond the end of the potential core, fluctuations will have penetrated into the core, causing unsteady location of the stagnation point, i.e. non-zero $\langle u'^2 \rangle$. Combined with the strong velocity gradient at the stagnation point, these fluctuations will cause high heat transfer. The dip in the Nusselt number will then disappear. Figure 26 illustrates this. Schematically, the path lines of two impinging jets are depicted, both with an eddy near their

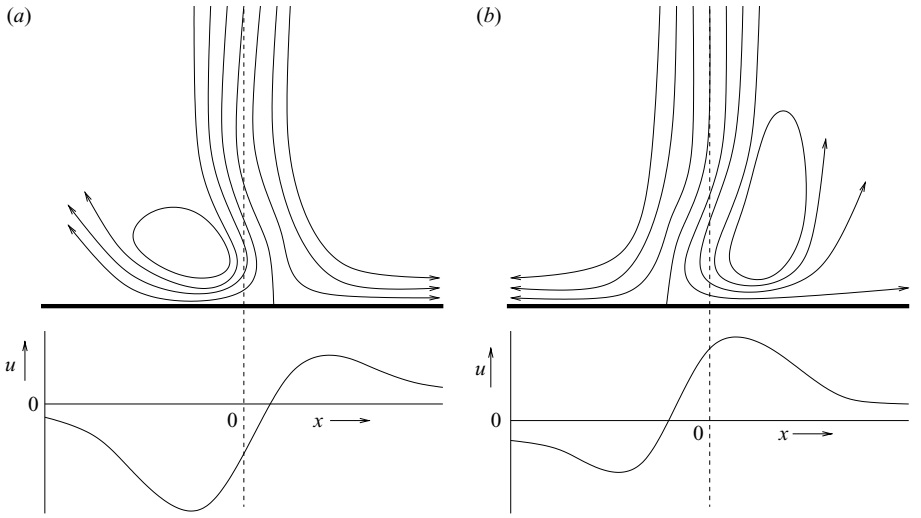

FIGURE 26. Sketched path lines of two impinging jets, each with an eddy near its impingement point and the corresponding near-wall velocity profiles along the impingement plate. (*a*) Eddy on the left side; (*b*) eddy on the right side.

impingement point, one on the left-hand side, one on the right-hand side. The charts below these figures depict the corresponding profiles of the velocity component along the impingement plate taken at a position just above the plate. The dashed line in both figures depicts the centrelines of the jets. An impinging eddy will cause a strong flow along the impingement plate. This will cause a high heat transfer rate. Because eddies will impinge on either side of a jet's centreline, the jet is swaying from one side to the other. Therefore, the instantaneous wall-parallel velocity component on the centreline is fluctuating strongly and heat is being removed efficiently. Even though the wall-parallel velocity is zero in the mean velocity field, the heat transfer rate will be high in the geometrical centre of the jet.

This contradicts the conjecture that the Nusselt number would be linked to regions of high k alone. The above described features also appear in figures 22, 23 and 24.

4. Conclusions

Liquid crystal measurements of surface heat transfer and particle imaging velocimetry of the flow field in impinging jet arrays with different orifice configurations have been performed to study effects of various parameters on the heat transfer and its correlation with the flow and turbulence structure. Considered were two representative jet arrangements, an in-line and a hexagonal, the latter with two different orifice shapes: sharp-edged and contoured, all for a range of Reynolds numbers, orifice spacings, and orifice-to-target-plate distances. Despite geometrical symmetry, for the in-line configuration elliptical impingement patterns were observed in the heat transfer of the neighbouring jets as a result of the jet distortion due to mutual jet interactions. The elliptical pattern was also detected for the centre jet, which has been related to the asymmetrical flow pattern just above the impingement plate caused by an embedded low-momentum vortex only on one side of the domain diagonal.

It was also found that jets gradually lose their identity in the downstream direction owing to mutual interaction and turbulence generated in the edge shear layers. After

impingement, jets transform into wall jets on the target plate, which collide and create an upwash fountain and recirculation in the region between the jets. A strong crossflow of spent air towards the outlet is created in the region close to the impingement plate creating horse-shoe vortices around the peripheral jets, sweeping fluid away, even causing the jets to break up and, thus, preventing the jets from reaching the target surface. This pattern leaves a thermal imprint on the surface, which determines the Nusselt number distribution. The heat transfer deteriorates and its distribution becomes more homogeneous with increasing orifice-to-plate spacing. The crossflow deforms the peripheral jets and diminishes jet impacting velocity. In addition, spent air mixes with fresh air, which diminishes the temperature difference between the impingement plate and the air. Both these mechanisms result in lower Nusselt numbers.

The effects of jet–jet interaction are especially strong for small orifice spacing. So, for $s/D_m = 2$, in both hexagonal arrangements, the heat transfer profiles reveal that impingement regions of the neighbouring jets are visibly displaced outwards as H/D_m is increased. This is a result of collision of the wall jets emerging from the impingement region, thus pushing the jets away from each other. The central jet, being stronger, imposes a crossflow of spent air pushing the neighbouring jet outwards. Because of the strong mixing as a result of these interactions, the Nusselt number shows a more homogeneous profile at high H/D_m than for the cases where $s/D_m > 4$. In those cases, the interactions are less strong, so the jets keep their identity up to high values of H/D_m.

The extent in which the Nusselt number deteriorates depends on the shape of the orifices. Compared to contoured orifices, sharp-edged orifices produce a higher centreline velocity, causing higher Nusselt numbers. On the other hand, the velocity decay in a jet from a sharp-edged orifice is stronger than in that from a contoured orifice, so the Nusselt numbers of a sharp-edged orifice jet decay more strongly with increasing orifice-to-plate distance. With increasing orifice-to-plate spacing, the difference in Nusselt numbers (both stagnation point and area-averaged) between both orifice shapes decreases, because the jets gradually 'forget' their initial conditions. The heat transfer appears to be maximized if the impingement plate is placed at the end of the potential core, because at this position, a high jet velocity is combined with a high degree of turbulence. If the distance is increased, both the velocity and the turbulence level drop and therefore the heat transfer drops.

In the stagnation regions, the Nusselt number shows maximum values, whereas the production of turbulence kinetic energy is negative. This apparent correlation is believed to be coincidental: we conjecture that the major cause of the increase in Nu is a very strong acceleration of the fluid from the centre of the jet outwards, combined with an oscillation of the impingement position owing to large eddies penetrating the stagnation zone. In the impingement point, the boundary layer is very thin and the temperature gradient is very steep, enabling impinging eddies to encapsulate and remove heat in an effective way.

This work was sponsored by the Technology Foundation STW of the Netherlands, TNO-TPD and Rademaker-Den Boer.

REFERENCES

Angioletti, M., Tommaso, R. M. D., Nino, E. & Ruoco, G. 2003 Simultaneous visualization of flow field and evaluation of local heat transfer by transitional impinging jets. *Intl J. Heat Mass Transfer* **46**, 1703–1713.

Arjocu, S. C. & Liburdy, J. A. 1999 Near surface characterization of an impinging elliptic jet array. *Trans. ASME* I: *J. Fluids Engng* **121**, 384–390.

Barata, J. M. M. 1996 Fountain flows produced by multiple impinging jets in a crossflow. *AIAA J.* **34**, 2523–2530.

Colucci, D. W. & Viskanta, R. 1996 Effect of nozzle geometry on local convective heat transfer to a confined impinging air jet. *Expl Thermal Fluid Sci.* **13**, 71–80.

Findlay, M. J., Salcudean, M. & Gartshore, I. S. 1999 Jets in a crossflow: effects of geometry and blowing ratio. *Trans. ASME* I: *J. Fluids Engng* **121**, 373–378.

Gamard, S., George, W. K., Jung, D. & Woodward, S. 2002 Application of a 'slice' proper orthogonal decomposition to the far field of an axisymmetric turbulent jet. *Phys. Fluids* **14**, 2515–2522.

Gardon, R. & Cobonpue, J. 1962 Heat transfer between a flat plate and jets of air impinging on it. In *International Developments in Heat Transfer*, pp. 454–460. ASME, New York.

Gau, C., Sheu, W. Y. & Shen, C. H. 1997 Impinging cooling flow and heat transfer under acoustic excitations. *Trans. ASME* C: *J. Heat Transfer* **119**, 810–816.

Geers, L. F. G., Tummers, M. J. & Hanjalić, K. 2004 Experimental investigation of impinging jet arrays. *Exps. Fluids* **36**, 946–958.

Goldstein, R. J. & Timmers, J. F. 1982 Visualization of heat transfer from arrays of impinging jets. *Intl J. Heat Mass Transfer* **25**, 1857–1868.

Gonzalez, R. C. & Woods, R. E. 2002 *Digital Image Processing*, 2nd edn. Prentice–Hall.

Hay, J. L. & Hollingsworth, D. K. 1996 A comparison of trichromic systems for use in the calibration of polymer-dispersed thermochromic liquid crystals. *Expl. Thermal Fluid Sci.* **12**, 1–12.

Holmes, P., Lumley, J. L. & Berkooz, G. 1996 *Turbulence, Coherent Structures, Dynamical Systems and Symmetry*. Cambridge University Press.

Janssen, L. P. B. M. & Warmoeskerken, M. M. C. G. 1991 *Transport Phenomena – Data Companion*, 2nd edn, DUM, Delft.

Jeong, J. & Hussain, F. 1995 On the identification of a vortex. *J. Fluid Mech.* **285**, 69–94.

Kasagi, N., Moffat, R. J. & Hirata, M. 2001 *Handbook of Flow Visualisation*, 2nd edn, chap. 8. Taylor & Francis.

Kataoka, K. 1990 Impingement heat transfer augmentation due to large scale eddies. In *Heat Transfer 1990* (ed. G. Hetsroni), *Proc. 9th Intl Heat Transfer Conf.* vol. 1, pp. 255–273. Hemisphere.

Kline, S. J. & McClintock, F. A. 1953 Describing uncertainties in single-sample experiments. *Mech. Engng* **75**, 3–8.

Liu, T. & Sullivan, J. 1996 Heat transfer and flow structures in an excited circular impinging jet. *Intl J. Heat Mass Transfer* **39**, 3695–3706.

Loève, M. M. 1955 *Probability Theory*. Van Nostrand.

Lumley, J. L. 1967 The structure of inhomogeneous turbulent flows. In *Atmospheric Turbulence and Radio Wave Propagation*, pp. 166–178. Nauka, Moscow.

Lytle, D. & Webb, B. W. 1991 Secondary heat transfer maxima for air jet impingement at low nozzle-to-plate spacings. In *Experimental Heat Transfer, Fluid Mechanics, and Thermodynamics* (ed. J. F. Keffer, R. K. Shah & E. N. Ganić), pp. 776–783. New York.

Martin, H. 1977 *Advances in Heat Transfer*, vol. 13, pp. 1–60. Academic.

Matsumoto, R., Ishihara, I., Yabe, T., Ikeda, K., Kikkawa, S. & Senda, M. 1999 Impingement heat transfer within arrays of circular jets including the effect of crossflow (AJTE99-6386). In *Proc. 5th ASME/JSME Joint Thermal Engng Conf.* (ed. T. W. Simon & M. Shoji), pp. 1–8. ASME.

Mehta, R. D. & Bradshaw, P. 1979 Design rules for small low speed wind tunnels. *Aeronaut. J.* pp. 443–449, technical note.

Mladin, E. C. & Zumbrunnen, D. A. 1997 Local convective heat transfer to submerged pulsating jets. *Intl J. Heat Mass Transfer* **40**, 3305–3321.

Moffat, R. J. 1990 Experimental heat transfer. In *Proc. 9th Intl Heat Transfer Conf.* (ed. G. Hetsroni), vol. 1, pp. 187–205. Hemisphere.

Popiel, C. O. & Boguslawski, L. 1986 Mass or heat transfer in impinging single, round jets emitted by a bell-shaped nozzle and sharp-ended orifice. In *Heat Transfer 1986* (ed. C. L. Tien, V. P. Carey & J. K. Ferrel), *Proc. 8th Intl Heat Transfer Conf.* vol. 3, pp. 1187–1192. Taylor & Francis.

Roksnoer, P. J., van Opdorp, C., Maes, J. W. F. M., de Keijser, M. & Weber, C. 1989 The effect of the asymmetric vortex in vertical VPE reactors on deposition nonuniformity. *J. Electrochem. Soc.* **136**, 2427–2431.

van Santen, H., Kleijn, C. R. & van den Akker, H. E. A. 2000 Symmetry breaking in a stagnation-flow cvd reactor. *J. Crystal Growth* **212**, 311–323.

Thielen, L., Jonker, H. J. J. & Hanjalić, K. 2003 Symmetry breaking of flow and heat transfer in multiple impinging jets. *Intl J. Heat Fluid Flow* **24**, 444–453.

Viskanta, R. 1993 Heat transfer to impinging isothermal gas and flame jets. *Expl Thermal Fluid Sci.* **6**, 111–134.